Spatial Organization of Multicellular Living Systems

by

Haiqian Yang

Submitted to the Department of Mechanical Engineering
in partial fulfillment of the requirements for the degree of

Master of Science in Mechanical Engineering

at the

MASSACHUSETTS INSTITUTE OF TECHNOLOGY

September 2022

© Massachusetts Institute of Technology 2022. All rights reserved.

Author . . . .
Department of Mechanical Engineering
July 5, 2022

Certified by . . . .
Ming Guo
Associate Professor of Mechanical Engineering
Thesis Supervisor

Accepted by . . . .
Nicolas G. Hadjiconstantinou
Professor of Mechanical Engineering
Graduate Officer

Spatial Organization of Multicellular Living Systems

by

Haiqian Yang

Submitted to the Department of Mechanical Engineering
on July 5, 2022, in partial fulfillment of the
requirements for the degree of
Master of Science in Mechanical Engineering

Abstract

Cells cooperate as groups to achieve functions at the tissue level, and specific structural characteristics emerge from the local organization of neighboring cells. Analogous to classical physics where transformations in the local structure give rises to phases and phase transitions, the changes in local structures in multicellular assemblies can be essential for a variety of vital processes including morphogenesis, wound healing, and cancer. In this work, we use the two invariants (volume J and shear γ) of the deformation tensor of Delaunay triangles as a pair of quantities to define the local microstates of multicellular living systems. In chapter 3, we develop configurational fingerprints based on these local structures, volume J and shear γ, and extract two parameters, namely the volumetric and shear order parameters, that are reflective of the transitions of local order in the systems. Theoretically, these two parameters form a complete and unique pair of signatures for the local structural order of a multicellular system. The evolution of these two order parameters offers a robust and experimentally accessible way to map the phase transitions in expanding cell monolayers, and during embryogenesis and invasion of epithelial spheroids. In chapter 4, We show by both simulations and experiments that the isotropic invariant J follows a $k-\Gamma$ distribution, and the isochoric invariant γ follows an exponential distribution. We further propose two temperature-like quantities for cell assemblies, in which sense we show the periphery of an extravasating epithelial monolayer is ‘hotter’ than the core.

Thesis Supervisor: Ming Guo
Title: Associate Professor of Mechanical Engineering

Acknowledgments

I thank my advisor Ming Guo who guides me into the field of the mechanics of multicellular systems. His enthusiasm for science influences me, and I am always impressed by his physical intuitions. I thank my collaborators, Max Bi, Adrian Pegoraro and Rohan Abeyaratne for their help and very insightful suggestions. Classes at MIT have been very thought-provoking, and I especially thank Mehran Kardar and Mathias Kolle for discussions and inspirations. I also want to thank my friends Liu Yang, Shun Zhang, Yulong Han and Wenhui Tang for their help and encouragement. Finally, I am lucky to have the unconditional support and love from my parents, and I cannot express my gratitude enough to them.

Contents

1 Introduction **15**

2 Materials and Methods **17**

2.1 The Volume and Shear Structure 17

2.2 Cell Culture and Microscopy 19

2.3 Simulation 20

2.4 Cell Tracking 21

2.5 Determine the Reference Area 21

2.6 3D Version of J and γ 21

3 The Volume and Shear Order **23**

3.1 Binary Mixtures 24

3.2 Simulated Epithelia 26

3.3 Ventral Furrow Formation 27

3.4 Maturation of Epithelia 29

3.5 Epithelial versus Mesenchymal Cell Monolayers 32

3.6 Invasive versus Non-invasive Epithelial Clusters 34

4 Probability Distributions of Volume and Shear **37**

4.1 Simulated Epithelia 38

4.2 Maturation of Epithelia 38

4.3 Extravasation into Open Space 41

5 Summary and Outlook **43**

A Lemmas **47**

B Supplementary Results **49**

List of Figures

2-1 (A) An arbitrary triangle is compared to an equilateral referential triangle. Delaunay triangulation of (B) a solid-like cell monolayer; (C) a fluid-like cell monolayer in simulation. The nodes are centers of cells. 18

3-1 Schematics and configurational fingerprints. (A) Schematics: by comparing particle or cell positions with the reference state of equilateral triangles, the $vol - shear$ configurational fingerprints can be calculated. (B) $[\ln(vol)]^2$ and $\ln(shear)$ with respect to two eigenvalues of deformation gradient λ_1 and λ_2 are symmetric. (C) Configurational fingerprints of fluid-like systems are scattered, while those of solid-like systems are compacted. 23

3-2 Φ_{vol} and Φ_{shear} can identify jamming transition in binary mixtures with harmonic potential. (A) Spatial distributions of *vol* and *shear* show that the system maintains amorphous configuration after jamming; (B) Φ_{vol} and Φ_{shear} as functions of density. Φ_{vol} converges to different nonzero values at different critical densities, determined by radius ratio; Φ_{shear} suddenly drops at a density around 0.8, exactly where a finite stress starts to show in these systems, indicating a jammed status. Simulations are performed with a density increment of 0.001, varying from 0.100 to 0.840, and 10 different random initial particle positions. (C) Pressure as a function of density. Upon jamming, pressure suddenly grows with increasing density. For $R/r = 1.4, 2.0, 3.0$, pressure starts to scale with density after density increases to ~ 0.8 and stress is $\sim 10^{-11}$, so in this system, the classical definition yields 10^{-11} as a threshold for pressure, above which the system is undergoing jamming transition, until it is finally jammed. (D)-(E) For systems showing a finite pressure, Φ_{vol} is nearly constant (D), and pressure scales with Φ_{shear} (E). 24

3-3 Φ_{shear} alone marks jamming transition in SPV model of confluent cell monolayers, while any large change in Φ_{vol} is prohibited due to confluency. (A) Spatial distribution of SI, $\ln(vol)$, $\ln(shear)$ of a jammed ($P_0 = 3.000, v_0 = 0$) and an unjammed system ($P_0 = 4.591, v_0 = 0$). (B) Phase diagram of Φ_{vol}, Φ_{shear}, $\overline{SI}$ as functions of P_0 and v_0. Red boundary: $SI = 3.813$, indicating where jamming occurs in this system; yellow boundary: $\Phi_{shear} = -2$. $\overline{SI}$ represents the median value of shape index and SI represents shape index here, which is defined as $SI = perimeter/\sqrt{area}$ of each cell. A regular hexagon has a shape index ~ 3.72 while a regular pentagon has a shape index ~ 3.81, and it was previously shown that a hexagon dominated tissue is solid-like, while fluidization is observed when $\overline{SI} \sim 3.81$ [9]. 26

3-4 Two distinct scaling regimes of Φ_{vol} and Φ_{shear} as functions of time during embryogenesis. (A) Fluorescent image of tissue configuration. The reference state is set to be the initial frame. Data is taken from Supplementary Materials of Ref. [6]. The triangulation mesh is generated by connecting centroid position of cells. Scale bar, 25 µm. (B)-(C) Low *vol* (B) and high *shear* (C) region gradually appear. (D) Abrupt changes in the scaling law of both order parameters are observed at time $\sim$ 200 s. 27

3-5 Influence of different reference configurations on the evolution of Φ_{vol} and Φ_{shear} during Drosophila embryogenesis. (A) Equilateral triangles; (B) a real configuration near the transition point, $\sim$ 200 s; (C) a real configuration when the system is the most disordered, 395 s. The volumetric and shear order parameters quantify the system-specific distance from the current configuration to the reference configuration, in terms of volumetric and shear deformations. 28

3-6 Φ_{vol} and Φ_{shear} identify three scaling regimes against increasing density, i.e. gas-like, liquid-like and solid-like states of epithelial cell monolayer. (A) Heterogeneity in both *vol* and *shear* decays with increasing cell density. Scale bar, 100 µm. (B) With increased cell density, both Φ_{vol} and Φ_{shear} first decrease following power law relations, at which stage comparably large Φ_{vol} and Φ_{shear} suggest that the system is reminiscent of a gas. The first critical transition point is indicated by the power-law slope change in Φ_{vol}, after which density fluctuations are constrained, while Φ_{shear} may still decrease following the same power law, indicating that the system is amorphous but incompressible, thus is reminiscent of a liquid; the second critical transition point is then reached indicated by the power-law slope change in Φ_{shear}, after which packing disorder is regulated at a finite value, which is analogous to an amorphous solid. (Inset) cell density increases with time. 29

3-7 Amorphous transition in Φ_{shear} vanishes in MCF-10A monolayer after induction of EMT. (A) Cell nuclei, triangle mesh, and distribution of *vol* and *shear* of both TGFβ1 treated and control group. Scale bar, 100 µm. (B) Density as a function of time. (C) Φ_{vol} and Φ_{shear} as functions of time. (D) Φ_{vol} and Φ_{shear} as functions of cell density. Changes in the scaling behavior of both Φ_{vol} and Φ_{shear} are evident in the control as density increases, while only a change in Φ_{vol} is observed in the $TGF\beta 1$ treated monolayer as cell density increases. Transitions in scaling behavior are annotated to mark changes in material phases. G: gas-like phase; L: liquid-like phase; S: solid-like phase. 33

3-8 Invasive epithelial spheroids have larger density variations but no significant difference in amorphousness. (A) Typical cell trajectories. (B)-(C) Typical spatial distribution of *vol* (B) and *shear* (C). Dash box: the protrusion has more dynamic cells, larger shear deformation but similar volumetric deformation compared to the core. Scale bar, 50 µm. (D) Φ_{vol} and Φ_{shear} of non-invasive ($n = 17$) and invasive spheroids ($n = 16$). While volumetric order is significantly higher for invasive spheroids, shear order for both invasive and non-invasive spheroids are similarly large. Both order parameters deviate far from face-centered cubic crystalline structure. Student's t-test is used to evaluate statistical difference. $* * * : p < 0.001$; ns: no significant difference. FCC: face-centered cubic crystal structure. (E) Fluorescent imaging of vimentin intermediate filaments and nuclei. Scale bar, 50 µm. 35

4-1 In simulated cell monolayers, (A) γ follows exponential distribution (the solid lines are exponential fit); (B) J follows $k-\Gamma$ distribution (the solid lines are $k-\Gamma$ fit). 38

4-2 (A) γ follows exponential distribution; (B) J follows $k-\Gamma$ distribution in MDCK epithelia. Solid lines are fitted curves. (C) Probability distribution of γ can be collapsed to a single master curve, confirming the exponential distribution of γ at all different cell densities. (D) Average value of $J - J_{min}$ as a function of the variance of J. The coefficient k of the $k - \Gamma$ distribution can be calculated by $k = (< J - J_{min} >^2)/{\sigma_J}^2$. The two lines mark $k = 1$ and $k = 6$ respectively. The total length of the observation is 164 hours. Color bar indicates a dimensionless pseudo time. 39

4-3 Evolution of the two effective temperatures (A) Θ_J and (B) Θ_γ as functions of cell number density ρ. 40

4-4 The periphery of an epithelia colony is 'hotter' compared to the jammed core. (A) Fluorescent image of MCF-10A cells migrating from a confluent confined space through a slit into an open space. The color of overlaid trajectories indicates the average speed of the cell. The cells on the edge move faster. (B)-(C) Probability density functions of J^* and γ. (D)-(E) Radial distribution of k and λ. (F)-(G) Spatial distributions of volume and shear temperatures. 41

B-1 Behavior of a sparse MDCK epithelial cell monolayer is analogous to the nucleation in sparse LJ system whose potential energy is dominating over kinetic energy, in terms of (A) particle/cell positions; (B) ln(*vol*) (C) ln(*shear*). With increased particle density, the discrete packs start to aggregate (D). These packs are dense (E), and well packed (F). 50

B-2 Brightfield images of (A) MCF-10A epithelia versus (B) MCF-10A epithelia after induction of EMT. 51

B-3 The variance of divergence of velocity field increases at the periphery of epithelial colony. 52

Citations to Previously Published Work:

Large portions of Chapters 1,2,3 and 5 have appeared in the following paper: Yang, H., Pegoraro, A. F., Han, Y., Tang, W., Abeyaratne, R., Bi, D., & Guo, M. (2021). Configurational fingerprints of multicellular living systems. Proceedings of the National Academy of Sciences, 118(44), e2109168118.

Chapter 4 is based on a manuscript in progress: Yang, H. et al., A Pair of Configurational Temperatures of Epithelia.

Chapter 1

Introduction

Cells interact and cooperate at length scales far above individuals [52, 27]; these long-ranged interactions help determine tissue-level material characteristics. The ability to tune these material characteristics is important for many multicellular physiological and pathological processes including embryogenesis [35, 6, 44], cancer invasion [22, 32], and wound healing [13]. In these vital processes in living systems [4, 9, 42], cells bear many of the hallmarks of a material phase transition [54]. In wound healing, for example, cells near the wound edge appear to undergo a solid-to-fluid transition, becoming highly migratory, leading the wound closure [13]. Another example is tumor metastasis: benign tumors can maintain a stable configuration for decades; in contrast, cancers might spread all over the body in a short time. In this sense, benign tumors are as rigid as solids, while cancers are rather amorphous like fluids and cells that escape the tumor mass behave more like a gas.

To quantitatively understand these behaviors of multicellular systems, efforts have been made mainly based on quantifying cell motion such as effective diffusivity, aligning and swirling patterns, or morphological parameters such as shape index and aspect ratio [9, 42, 55, 51, 57, 59, 49, 62, 3, 38, 60, 20, 17, 50, 40, 10, 58]; yet, what order parameters are suitable to describe phase transitions in multicellular systems remain elusive [36]. This is in contrast to classical condensed matter theory where material rigidity is a direct consequence of local spatial order establishment among neighboring particles, a concept has not previously been explored in living systems.

In solid mechanics, classical constitutive material relations are defined in terms of volumetric and shear deformations, which describe the change in structure among neighboring material points [29]. Thus, defining volume and shear structures in multicellular systems may allow us to establish more general framework for multicellular assemblies that are more directly related to classical mechanical characteristics. Here we show that volumetric and shear structures can be defined for amorphous systems and changes in these parameters are reflective of phase transitions in both particulate and multicellular systems.

Chapter 2

Materials and Methods

2.1 The Volume and Shear Structure

In thermal systems, the energy competition between isotropic (volumetric) and isochoric (shear) deformation identifies three distinct phases (i.e. gas, liquid, solid). Gas can barely resist volumetric or shear deformation while solid resists both. In between, liquid is often considered as resistant only to volumetric deformation. Theoretically, the isotropic and isochoric invariants of deformation are a pair of mutually independent and complete variables that can fully quantify the local deformation. In 2D, three noncollinear adjacent cells form a triangle. Assuming N triangles can be formed by linking adjacent cells, the n-th triangle ($n = 1, 2, ..., N$) in current configuration can be expressed as a matrix $\mathbf{T_n} = \begin{pmatrix} X_{n1} - X_{n0} & X_{n2} - X_{n0} \\ Y_{n1} - Y_{n0} & Y_{n2} - Y_{n0} \end{pmatrix}$ [Fig. 2-1A] , where X_{nm}, Y_{nm} ($m = 0, 1, 2$) are Cartesian coordinates of the m-th vertice of the n-th triangle. This segmentation method is known as Delaunay triangulation, and has been previously used to measure strain for granular materials [7], and during biological tissue development [21, 26].

Here, instead of measuring strains, we seek to quantify the degree of disorder of the system at one point in time by comparing to an ideal reference frame. We consider the reference triangle to be the most regular and special one, an equilateral

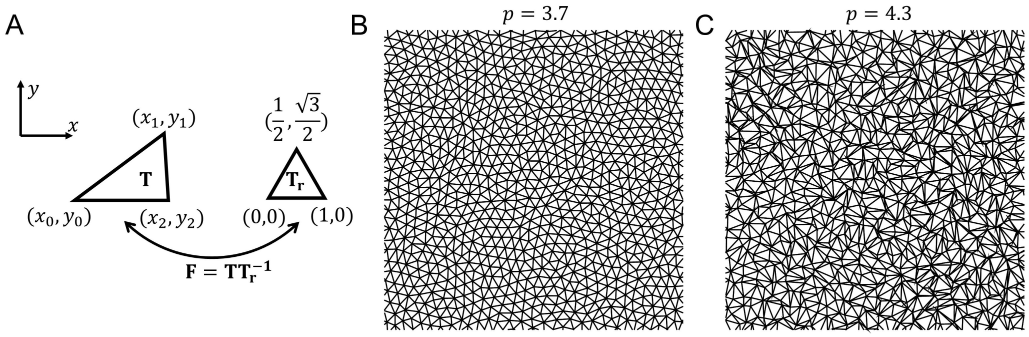

Figure 2-1: (A) An arbitrary triangle is compared to an equilateral referential triangle. Delaunay triangulation of (B) a solid-like cell monolayer; (C) a fluid-like cell monolayer in simulation. The nodes are centers of cells.

triangle with $\mathbf{T_r} = \sqrt{A}\begin{pmatrix} 1 & \frac{1}{2} \\ 0 & \frac{\sqrt{3}}{2} \end{pmatrix}$ (Fig. 2-1A), where $\frac{\sqrt{3}}{4}A$ is the average area of all Delaunay triangles. The triangle matrix $\mathbf{T}$ has 4 elements but not all these elements are independent state variables. The following arguments should be considered:

i) The microstates should not depend on the orientation of coordinate system.

ii) For an isotropic system, congruent triangles should be at the same microstate.

These two arguments are similar to the *material frame indifference* and *isotropic material symmetry* typically considered in continuum mechanics, and can be achieved by considering the invariants of the Cauchy-Green deformation tensor. The corresponding deformation gradient is $\mathbf{F_n} = \mathbf{T_n}\mathbf{T_r}^{\mathbf{-1}}$. A pair of independent and complete invariants are $J = det(\mathbf{F})$ and $\gamma = \frac{tr(\mathbf{F^T F})}{det(\mathbf{F})} - 2$, which reflect how much area each triangle deviates from the average area and how much distortion each triangle has compared to the equilateral ones, respectively. It can be proved that the two deformations are independent of orientation of the reference triangle (Lemma 1 in Appendix A). Tiling up a surface with equilateral triangles results in hexagonal packing, which is found to be the most frequent cell packing in simple epithelia [24]. Let λ_i $(i = 1, 2)$ be principal stretches. It can be proved that any deformation gradient $\mathbf{F}$ can be factored as $\mathbf{F} = \mathbf{F_v}\mathbf{F_s}$, where $\mathbf{F_v}$ is a volumetric deformation with equivalent amount of stretch $v = (\lambda_1\lambda_2)^{1/2}$, and $\mathbf{F_s}$ is a simple shear with equivalent amount of shear $s = \sqrt{\lambda_1/\lambda_2} - \sqrt{\lambda_2/\lambda_1}$; moreover, J and γ represent the real volumetric and shear deformations of each triangle by $J = v^2$ and $\gamma = s^2$ (Lemma 2 in Appendix A).

2.2 Cell Culture and Microscopy

Madin-Darby Canine Kidney (MDCK) Monolayer. MDCK cells were stably transfected with green fluorescent protein tagged with nuclear localization signal (GFP-NLS). Cells were cultured and imaged at 37 °C and 5% CO_2 -in Dulbecco's modified Eagle's medium supplemented with 10% fetal bovine serum, 1% penicillin/streptomycin and $0.5\,\mathrm{mg\,mL^{-1}}$ G418. Rat tail collagen I ($3\,\mathrm{mg\,mL^{-1}}$) was diluted to $0.1\,\mathrm{mg\,mL^{-1}}$ in phosphate buffered saline (PBS) and used to coat 12-well tissue culture plates prior to seeding. 50,000 cells were added per well and allowed to adhere for 24h prior to imaging. All images were recorded on a Leica SP5 confocal microscope using 10× magnification and using the 488 nm line of an argon ion laser. Cells were maintained in a stage top live cell incubation chamber for the duration of imaging. Both phase (cell boundaries) and fluorescence (GFP, cell nuclei) channels were recorded simultaneously every 3 minutes for 64 hours.

MCF-10A. MCF-10A cells were transfected with GFP-NLS. Cells were cultured following a previously established protocol [18]. Briefly, cells were cultured and imaged at 37 °C and 5% CO_2 -in Dulbecco's modified Eagle's medium/F-12 supplemented with 5% horse serum, $20\,\mathrm{ng\,mL^{-1}}$ epidermal growth factor, $0.5\,\mathrm{\mu g\,mL^{-1}}$ hydrocortisone, $100\,\mathrm{ng\,mL^{-1}}$ cholera toxin, $10\,\mathrm{\mu g\,mL^{-1}}$ insulin, and 1% penicillin and streptomycin.

The Epithelial Mesenchymal Transition (EMT) Treatment and Microscopy of MCF-10A Monolayer. The EMT group was cultured with the medium supplemented with $10\,\mathrm{ng\,mL^{-1}}$ TGFβ1 (PN:90900-1, BPS Bioscience, San Diego, CA, USA) for 1 week prior to and throughout the measurement. Bovine collagen I ($10\,\mathrm{mg\,mL^{-1}}$) was diluted to $0.1\,\mathrm{mg\,mL^{-1}}$ in PBS and used to coat a 6-well tissue culture plate prior to seeding. Each group was seeded in three wells. All images were recorded on a Leica SP8 confocal microscope using 10× magnification and 488 nm excitation. 14 positions of each group were imaged starting from 12 hours after seeding and every 12 hours afterwards for 156 hours.

3D Cell Culture and Microscopy of MCF-10A Spheroids. MCF-10A cells were grown in an interpenetrating gel containing $5\,\mathrm{mg\,mL^{-1}}$ alginate and $4\,\mathrm{mg\,mL^{-1}}$ Matrigel. All images were recorded on a Leica SP8 confocal microscope.

Immunofluorescent Staining. Normal MCF-10A cells (without GFP-NLS) are seeded in the same 3D gel. The 3D gel with spheroids were fixed with 4% paraformaldehyde for 30 minutes, immersed in 0.2% Triton X-100 in PBS for 2 hours, and blocked with 0.5% bovine serum albumin (BSA) in PBS for 5 hours at room temperature. The sample was then incubated with primary antibodies for vimentin (1:300 diluted in PBS, Santa Cruz Biotechnology, sc-6260) at 4 °C overnight, with the secondary antibody (Alexa Fluor 488 goat anti-mouse IgG (H+L), 1:1000) at 4 °C overnight, and stained with DAPI (ThermoFisher, D1306) for one hour. The sample was washed with PBS for 6 hours between each step.

2.3 Simulation

Simulation of Binary Mixture. The particles interact with each other through an one sided harmonic potential energy $U_b(d) = \frac{1}{2}(\frac{r_i+r_j}{d} - 1)^2 R(\frac{r_i+r_j}{d} - 1)$, where $R(x) = \begin{cases} 1 & x > 0 \\ 0 & x \leq 0 \end{cases}$ is a step function, r_i and r_j are radius of two interacting particles respectively, and d is the distance between the two particles. 256 particles of radius R and 256 particles of radius r are initially randomly distributed. A system energy tolerance is set to be 10^{-8} to reach equilibrium. The simulation box is set to have unit length. The simulations are done with self-made MATLAB codes. FIRE minimization algorithm is used [11].

The stress tensor is given by [1] $\boldsymbol{\sigma} = \frac{1}{V}\sum_{i \neq j} \boldsymbol{x}^{ij} \otimes \boldsymbol{f}^{ij}$, where $\boldsymbol{x}^{ij} = \boldsymbol{x}^i - \boldsymbol{x}^j$ is the difference of the position vectors of grain i and grain j, $V = 1$ is the volume of the simulation box, “ $\otimes$ ” denotes a vector outer product, and the force vector is given by $\boldsymbol{f}^{ij} = -(|\boldsymbol{x}^{ij}| - r_i - r_j)\frac{\boldsymbol{x}^{ij}}{|\boldsymbol{x}^{ij}|}R(\frac{r_i+r_j}{|\boldsymbol{x}^{ij}|} - 1)$.

Simulation of Confluent Cell Monolayers. The self-propelled Voronoi (SPV) simulation is performed following the methods in [10]. Briefly, SPV model has a system energy of N Voronoi cells composed of quadratic functions of the area and perimeter of cells, $E = \sum_{i=1}^{N} K_A(A_i - A_0)^2 + K_P(P_i - P_0)^2$, where A_i and P_i are area and perimeter of the i-th cell, A_0 and P_0 are their preferred area and perimeter, K_A and K_P are the area and perimeter moduli. Position $\boldsymbol{r_i}(t)$ and polarity angle $\theta_i(t)$ of each individual cell at arbitrary time t are governed by $\frac{\partial \boldsymbol{r_i}}{\partial t} = \mu \boldsymbol{F_i} + \nu_0 \boldsymbol{n_i}$ and $\frac{\partial \theta_i}{\partial t} = \eta_i(t)$, where $F_i = -\frac{\partial E}{\partial r_i}$, $n_i = (cos\theta_i \ \ sin\theta_i)$ is the polarity vector of the cell, $\eta_i(t)$ is a white noise with zero mean and variance $2D$ that follows $< \eta_i(t)\eta_j(t') >= 2D\delta(t-t')\delta_{ij}$, μ is the mobility, and v_0 is a self-propelling coefficient. The demonstration in Fig. 3-3A is simulated with 2500 Voronoi cells, and the parametric study in Fig. 3-3B is performed with 400 Voronoi cells.

2.4 Cell Tracking

Cell tracking is performed with TrackMate in ImageJ [53].

2.5 Determine the Reference Area

Considering a hexagonal lattice with N vertices, since most vertices are shared by 6 triangles and every triangle has 3 vertices, the reference area $\frac{\sqrt{3}}{4}A$ thus can be estimated by $\frac{A_{total}}{2N}$, where A_{total} is the total area of the field of view. A proper reference area can be verified by confirming that $< vol >\sim 1$.

2.6 3D Version of J and γ

In 3D, four nonplanar adjacent cells form a tetrahedron. Assuming N tetrahedrons can be formed by linking adjacent cells, the n-th tetrahedron ($n = 1, 2, ..., N$) can be expressed as a matrix $\mathbf{T_n} = \begin{pmatrix} X_{n1} - X_{n0} & X_{n2} - X_{n0} & X_{n3} - X_{n0} \\ Y_{n1} - Y_{n0} & Y_{n2} - Y_{n0} & Y_{n3} - Y_{n0} \\ Z_{n1} - Z_{n0} & Z_{n2} - Z_{n0} & Z_{n3} - Z_{n0} \end{pmatrix}$, where X_{nm}, Y_{nm} ($m = 0, 1, 2, 3$) are Cartesian coordinates of the m-th vertice of the n-th tetrahedron. We assume the reference state to be equilateral tetrahedrons, which gives the unit reference state $\mathbf{T_0} = \begin{pmatrix} 1 & \frac{1}{2} & \frac{1}{2} \\ 0 & \frac{\sqrt{3}}{2} & \frac{\sqrt{3}}{6} \\ 0 & 0 & \frac{\sqrt{6}}{3} \end{pmatrix}$. The corresponding deformation gradient is $\mathbf{F_n} = \mathbf{T_n}\mathbf{T_0^{-1}}$. Similar to 2D, we have $v^3 = det(\mathbf{F})$, and $s^3 = \frac{tr(\mathbf{F^T F})}{det(\mathbf{F})^{2/3}} - 3$. We further define $J_0 = v^3$, and $\gamma = s^3$. The reference volume $(\overline{J_0})$ can be estimated by the median value of J_0 of all tetrahedrons. Further, J is defined by $J = \frac{J_0}{\overline{J_0}}$.

Moreover, rather than forming tetrahedrons in a way similar to forming Delaunay triangles, we apply an averaging method described below to reduce noise. For each cell, we define it together with p most adjacent cells to be the neighboring subset on that cell. Within this subset, we form all possible tetrahedrons, and use the median values of J_0 and γ as the representative values of the neighboring subset on that cell. p is set to be 5 in the current study.

Particle positions of a 11×11×11 face-centered cubic crystal is generated for comparison in Fig. 3-8D.

Chapter 3

The Volume and Shear Order

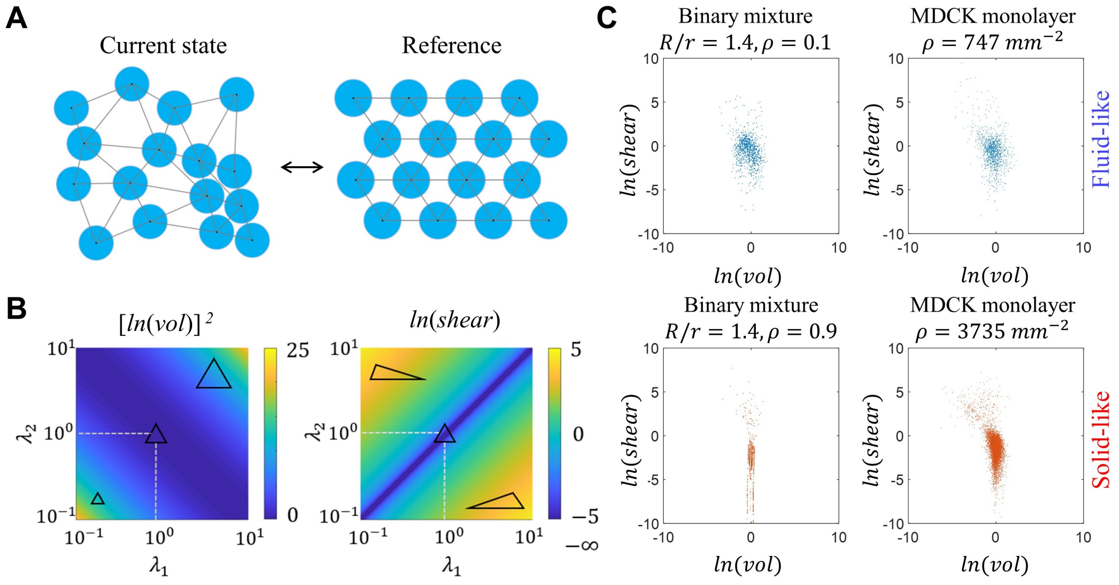

Figure 3-1: Schematics and configurational fingerprints. (A) Schematics: by comparing particle or cell positions with the reference state of equilateral triangles, the $vol-shear$ configurational fingerprints can be calculated. (B) $[\ln(vol)]^2$ and $\ln(shear)$ with respect to two eigenvalues of deformation gradient λ_1 and λ_2 are symmetric. (C) Configurational fingerprints of fluid-like systems are scattered, while those of solid-like systems are compacted.

The volume $vol \overset{\text{def}}{=} J$ and shear $shear \overset{\text{def}}{=} \gamma$ quantifies the local structure in a system: If we plot $\ln(vol)$ and $\ln(shear)$ of all triangles within a system, it generates a unique configurational fingerprint (Fig. 3-1C). Two characteristics can be identified from the configurational fingerprints, one is the horizontal width of the fingerprint that reflects the degree of density variation across the whole sample, and the other is the mean vertical position of the fingerprint that reflects how regular these triangles are. To quantify the density variation, we define the volumetric order parameter as $\Phi_{vol} =< [\ln(vol_n)]^2 >$; to quantify the average degree of amorphousness, we define the shear order parameter as $\Phi_{shear} =< \ln(shear_n)^2 >$, where $<>$ is the ensemble average of all triangles.

3.1 Binary Mixtures

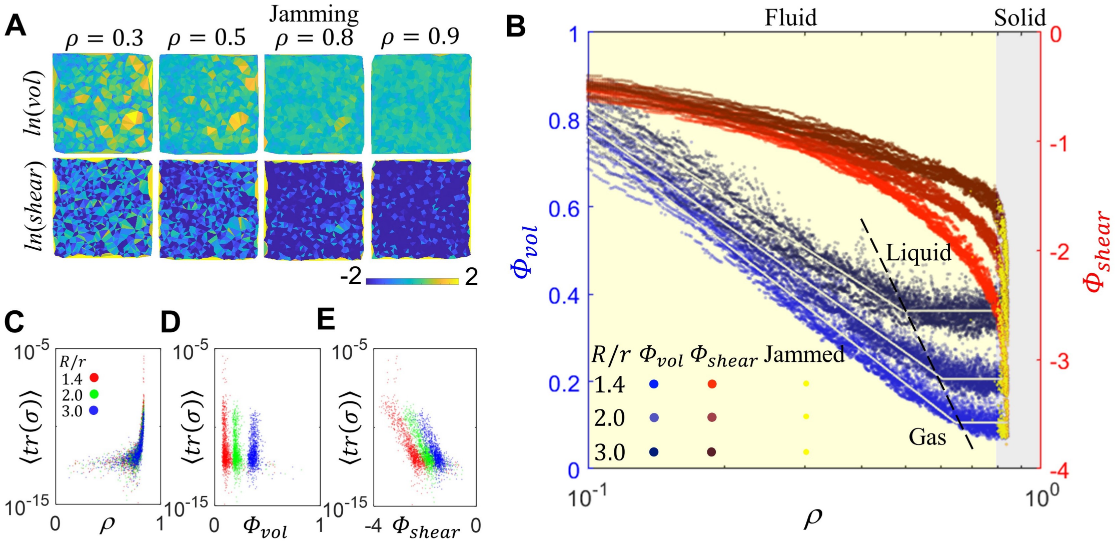

Figure 3-2: Φ_{vol} and Φ_{shear} can identify jamming transition in binary mixtures with harmonic potential. (A) Spatial distributions of *vol* and *shear* show that the system maintains amorphous configuration after jamming; (B) Φ_{vol} and Φ_{shear} as functions of density. Φ_{vol} converges to different nonzero values at different critical densities, determined by radius ratio; Φ_{shear} suddenly drops at a density around 0.8, exactly where a finite stress starts to show in these systems, indicating a jammed status. Simulations are performed with a density increment of 0.001, varying from 0.100 to 0.840, and 10 different random initial particle positions. (C) Pressure as a function of density. Upon jamming, pressure suddenly grows with increasing density. For $R/r = 1.4, 2.0, 3.0$, pressure starts to scale with density after density increases to ~ 0.8 and stress is $\sim 10^{-11}$, so in this system, the classical definition yields 10^{-11} as a threshold for pressure, above which the system is undergoing jamming transition, until it is finally jammed. (D)-(E) For systems showing a finite pressure, Φ_{vol} is nearly constant (D), and pressure scales with Φ_{shear} (E).

To examine these two order parameters in classical thermal systems, we study the jamming transition of amorphous materials in simulation of 2D binary mixtures with harmonic repulsive potentials [39, 46]. We simulate three systems with different binary size ratios and increase particle density to reach jamming. As we calculate the volumetric and shear deformations, we find that both types of deformation remain non-zero and highly heterogeneous even at very high densities (Fig. 3-2A). Examining the order parameters, we see at low particle densities a large Φ_{vol} that reflects significant density fluctuations, indicating that the system is compressible, which is a distinctive characteristic of gas. With increasing density, we find that Φ_{vol} eventually stabilizes at a finite value above zero even as particle density increases further (Fig. 3-2B), which is reminiscent of a relatively incompressible amorphous condensed phase. Further increasing density above the first transition point where Φ_{vol} stabilizes, Φ_{shear} continuously decreases, indicating that the system becomes more ordered in packing but maintains a constant density fluctuation, which are characteristics of a liquid. With even higher density, a second transition point occurs with a sudden decrease of Φ_{shear}. This sudden change in packing order indicates that the system is jammed and becomes solid-like. In addition, the diverging Φ_{shear} might be related to the diverging viscosity at jamming [54, 41, 45, 31]. Moreover, jamming is classically defined as systems showing a finite pressure. Interestingly, we find that while Φ_{vol} remains roughly unchanged (Fig. 3-2D), Φ_{shear} scales with pressure (Fig. 3-2E). This result suggests that rigidity transition in this system is characterized by regulation in packing disorder, Φ_{shear}. Furthermore, this constitutive relationship between Φ_{shear} and pressure should allow the stress at particle interfaces to be calculated by the measured deformations. If this approach was applied to cellular systems, it would be reminiscent of previous work that has shown that relative values of cell-cell tensions can be inferred from static images of confluent cell monolayer by assuming a foam-like structure [56].

3.2 Simulated Epithelia

To benchmark this framework in confluent living systems, as opposed to particulate systems, we first investigate the jamming process of a SPV model system of confluent cells at different preferred cell perimeter P_0 and self-propelling velocity v_0 (Fig. 3-3), following the methods described previously [10]. Compared to the jammed state, unjammed state has a highly heterogeneous spatial distribution of vol and $shear$, which is consistent with shape index (SI) (Fig. 3-3A). Using our new framework, a sharp transition in Φ_{shear} is observed as the system evolves (Yellow boundary, $\Phi_{shear} = -2$, Fig. 3-3B), which is consistent with the phase boundary given by the median value of shape index ($\overline{SI}$) (Red boundary, $\overline{SI} = 3.813$, Fig. 3-3B). Because this simulated system is fully confluent with constant cell number, although Φ_{vol} slowly increases with increasing P_0 or v_0, no sharp transition is observed throughout the simulation.

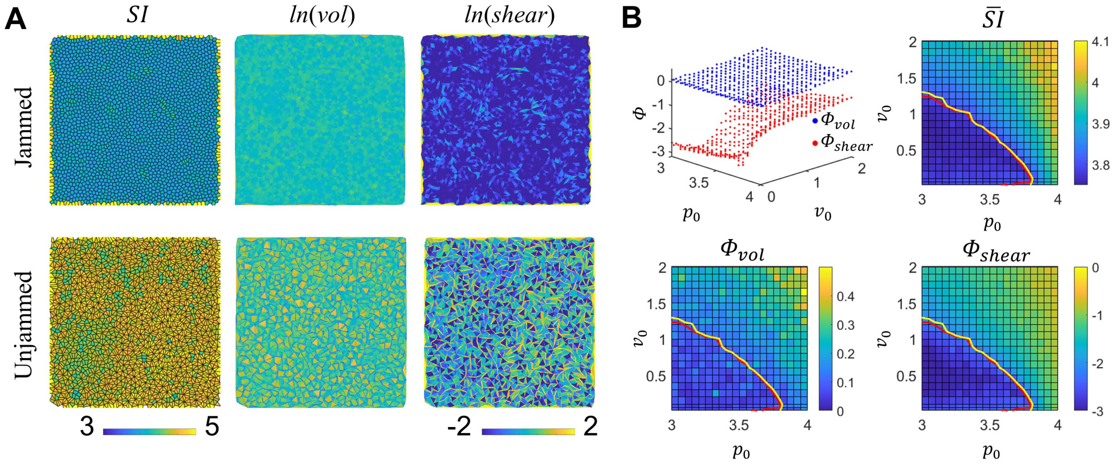

Figure 3-3: Φ_{shear} alone marks jamming transition in SPV model of confluent cell monolayers, while any large change in Φ_{vol} is prohibited due to confluency. (A) Spatial distribution of SI, $\ln(vol)$, $\ln(shear)$ of a jammed ($P_0 = 3.000, v_0 = 0$) and an unjammed system ($P_0 = 4.591, v_0 = 0$). (B) Phase diagram of Φ_{vol}, Φ_{shear}, $\overline{SI}$ as functions of P_0 and v_0. Red boundary: $SI = 3.813$, indicating where jamming occurs in this system; yellow boundary: $\Phi_{shear} = -2$. $\overline{SI}$ represents the median value of shape index and SI represents shape index here, which is defined as $SI = perimeter/\sqrt{area}$ of each cell. A regular hexagon has a shape index ~ 3.72 while a regular pentagon has a shape index ~ 3.81, and it was previously shown that a hexagon dominated tissue is solid-like, while fluidization is observed when $\overline{SI} \sim 3.81$ [9].

3.3 Ventral Furrow Formation

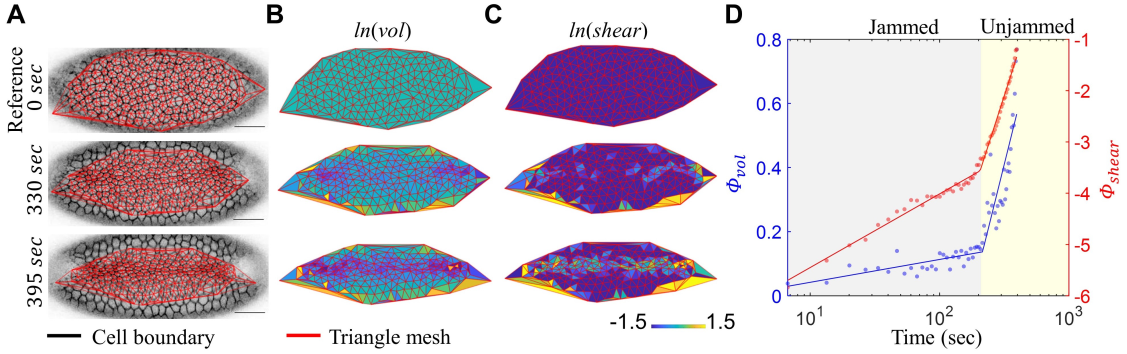

Figure 3-4: Two distinct scaling regimes of Φ_{vol} and Φ_{shear} as functions of time during embryogenesis. (A) Fluorescent image of tissue configuration. The reference state is set to be the initial frame. Data is taken from Supplementary Materials of Ref. [6]. The triangulation mesh is generated by connecting centroid position of cells. Scale bar, 25 µm. (B)-(C) Low *vol* (B) and high *shear* (C) region gradually appear. (D) Abrupt changes in the scaling law of both order parameters are observed at time ~ 200 s.

We then analyze confluent multicellular systems from a 2D case with a clear macroscopic pattern, the ventral furrow formation during morphogenesis of Drosophila germband epithelium (Fig. 3-4). The ventral furrow formation is known to be accompanied by elongation of individual cells in the central region, as can be measured from cell aspect ratios [6]. Elongated individual cells however, do not necessarily lead to changes in spatial order of cells as a collective. Here we report that this process displays a clear pattern of changes in relative spatial relation among neighboring cells, that the central region is not only shearing but also shrinking (Figs. 3-4B&C). More interestingly, both power-law relationships of Φ_{shear} and Φ_{vol} as functions of time are abruptly changed at ~ 200 s, as the ventral furrow forms and cell number density changes. The evolution in Φ_{shear} and Φ_{vol} includes two successive but distinct phases: in the first phase, both Φ_{shear} and Φ_{vol} change slowly and the system behaves like jammed, while in the second phase, both Φ_{shear} and Φ_{vol} change rapidly, indicating that the system undergoes unjamming transition. It is worth noting, however, that these changes could be due to other mechanisms instead of material phase transitions. For example, a mechanical instability can potentially be responsible for this unjammed zone as well; creasing instability, which has been used to explain the formation of sulci biological tissues [28], might happen when homogeneous solid film is under in plane compression, where a huge amount of deformation energy is released in one narrow but severely deformed zone. Nonetheless, the order parameters capture the dramatic change in structural order that occurs during this process.

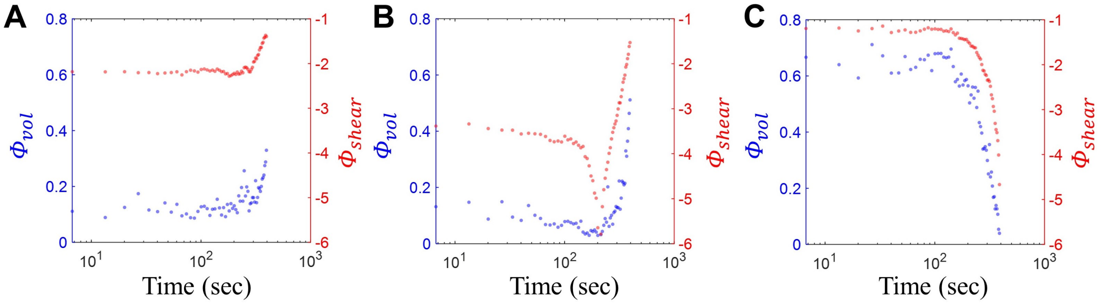

Figure 3-5: Influence of different reference configurations on the evolution of Φ_{vol} and Φ_{shear} during Drosophila embryogenesis. (A) Equilateral triangles; (B) a real configuration near the transition point, $\sim$ 200 s; (C) a real configuration when the system is the most disordered, 395 s. The volumetric and shear order parameters quantify the system-specific distance from the current configuration to the reference configuration, in terms of volumetric and shear deformations.

The volumetric and shear order parameters essentially quantify the system-specific distances from the current state to the reference state; they increase as the system configuration deviates from the reference state. In the current study, the reference configurations are mostly assumed to be equilateral triangles. Consequently, the configuration having the most congruent and equilateral triangles will have the smallest value of both order parameters. In less-controlled situations, this equilateral shape may still serve as a reasonable reference, while system configurations within a certain distance to it might not be achievable due to factors such as intrinsic size variation within the population, asynchronous shrinking and swelling of cells, naturally anisotropic tissue, or substrate curvature. In these situations, other reference configurations may reveal more details. For instance, in the embryogenesis example (Fig. 3-4), the reference state is taken as the initial frame where no global pattern is distinguishable from the image, and this allows *vol* and *shear* to precisely reflect the deformation compared to the initial frame. In some other situations, the reference state can be set at the critical transition point, and the order parameters would reflect the system-specific distances from the transition point (Fig. 3-5). Although these alternative references may provide other useful information, they require that a real configuration of each sample be identified as the reference. This might bring extra complications when applying to complex processes taking place on a comparably long timescale. Furthermore, sample specific reference states make it especially challenging to compare across different samples. By contrast, using equilateral triangles as reference is simple and general, especially when studying noisy data such as clinical samples.

3.4 Maturation of Epithelia

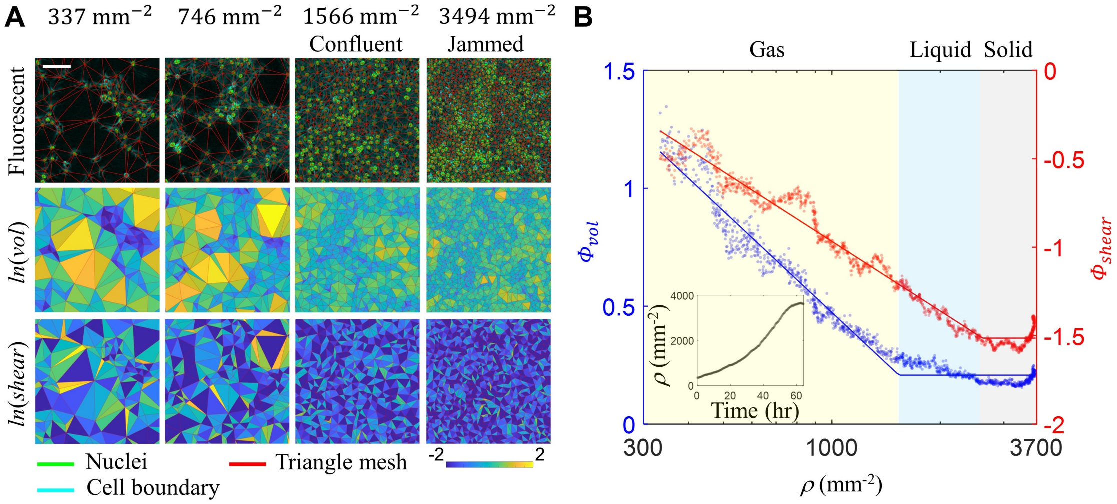

Figure 3-6: Φ_{vol} and Φ_{shear} identify three scaling regimes against increasing density, i.e. gas-like, liquid-like and solid-like states of epithelial cell monolayer. (A) Heterogeneity in both vol and $shear$ decays with increasing cell density. Scale bar, 100 µm. (B) With increased cell density, both Φ_{vol} and Φ_{shear} first decrease following power law relations, at which stage comparably large Φ_{vol} and Φ_{shear} suggest that the system is reminiscent of a gas. The first critical transition point is indicated by the power-law slope change in Φ_{vol}, after which density fluctuations are constrained, while Φ_{shear} may still decrease following the same power law, indicating that the system is amorphous but incompressible, thus is reminiscent of a liquid; the second critical transition point is then reached indicated by the power-law slope change in Φ_{shear}, after which packing disorder is regulated at a finite value, which is analogous to an amorphous solid. (Inset) cell density increases with time.

While confluent cellular systems widely exist, there are many multicellular systems that are non-confluent, which can also be critical in various physiological and pathological processes; for example, in cancer metastasis, individual cells can escape from the tumor mass. The transition from non-confluency to confluency might, although not necessarily, lead to a transition in density fluctuation, which is a widely used signature of liquid-gas transition in classical systems [48, 61]. Here we show that in addition to the liquid-solid jamming transition in confluent systems detected by Φ_{shear}, Φ_{vol} further captures this transition of density fluctuation in living systems and defines two distinct phases reminiscent of gas and liquid.

We apply this method to the process of sparsely distributed epithelial cells on 2D forming a confluent monolayer. Previous studies have shown that fluid-solid phase transitions exist in 2D monolayers, as quantified by individual cell dynamics [4], cell shape index [9] and aspect ratio [6]. Yet, as sparsely migrating cells behave reminiscent of a gas phase, it has not been distinguished from liquid phase in 2D multicellular systems, possibly due to the lack of proper order parameters that can consistently describe multicellular systems below confluency. Here we show that this gap can be filled by Φ_{vol}; Φ_{vol} and Φ_{shear} together capture the full picture of the transformation from gas, to liquid and finally to amorphous solid of a growing epithelial monolayer. To do so, we culture MDCK cells on a 2D glass substrate coated with collagen I, allowing them to divide and increase in density. Cells are initially seeded at a very dispersed state, and they gradually reach confluency and approach jamming as density increases (Fig. 3-6A top). We image this entire process every 3 min using confocal microscopy. Cells are transfected with GFP-NLS that allows us to see individual nuclei, which we use to calculate the volumetric and shear order parameters of the system. Initially, comparably large Φ_{vol} and Φ_{shear} show significant density fluctuations as well as random arrangement among cells, suggesting a gas-like state. Then the volumetric and shear deformations are simultaneously and gradually restricted following a power-law relation, until Φ_{vol} first reaches its inflection point (Fig. 3-6B). This inflection point occurs when the monolayer reaches confluency, with a density around $1500\,\mathrm{mm}^{-2}$, at which density fluctuation is stabilized, indicating that the cells behave like a relatively incompressible but amorphous liquid. Beyond this point, Φ_{vol} becomes comparably stable, and Φ_{shear} continues to decrease, suggesting that further decrease in the volumetric fluctuation is significantly hindered but packing disorder is still reduced with increasing density, which is reminiscent of liquid to solid transition, consistent with our simulation of confluent monolayers (Fig. 3-3). Interestingly, unlike the behaviors of those binary mixtures that the stabilized Φ_{vol} is almost unchanged above the first transition point (Fig. 3-2), a small decrease can still be observed in the volume fluctuation Φ_{vol} of a cell monolayer (Fig. 3-6B), although changing at a comparably slower rate compared to the gas state. This is similar to the jammed phase of the embryo (Fig. 3-4), where the cells start to slowly deform. The rate of changes in Φ_{vol} in the jammed state thus may reflect deformability of the monolayer. The second inflection point is identified by Φ_{shear} which marks the endpoint of the fluid phase, at a density $\sim 2600\,\mathrm{mm}^{-2}$, after which both Φ_{vol} and Φ_{shear} do not further decrease, indicating a jammed state; this critical density ($\sim 2800\,\mathrm{mm}^{-2}$) is consistent with previous report in MDCK monolayer identified based on significantly reduced cell speed and increased pack size [4].

Furthermore, results in the gas-liquid transition regime also reveal that these adhesive epithelial cells develop spatial order long before they are connected into a complete monolayer. Indeed, below confluency, rather than evenly distributed, cells form packs with void regions among these packs, as can be seen from the microscopic images (Fig. 3-6A top). This is analogous to nucleation of sparse adhesive particles whose potential energy is dominating over kinetic energy (Figs. B-1A-C); with higher density, these packs aggregate into larger ones (Figs. B-1D-F). Interestingly, while cells in the packs are more elongated and polarized below confluency, their shapes gradually become more isotropic with increasing density. Moreover, similar to the binary mixture, the stabilized Φ_{vol} is nonzero, suggesting an intrinsic disorder in the monolayer. Since the monolayer is already confluent at this stage, this is possibly resulted from volume fluctuation of individual cells. Besides the natural difference among individuals, this may be due to cell division, or asynchronous swelling and shrinking during cell cycle. For different systems, perturbing the degree of this volume heterogeneity may also influence the critical transition points. As a minimal model, the binary systems of different binary ratio have different level of size fluctuations, and systems with larger size fluctuations exhibit a shift of the first transition point to lower density (Fig. 3-2B). The spatial distributions of local volumetric and shear deformations show that the system gradually becomes more homogeneous as the monolayer approaches jamming (Fig. 3-6A). Additionally, the evolution of the two order parameters in the liquid-solid transition regime suggests that it is not restrictions on volumetric deformations but rather on shear deformations that drive this liquid to solid transition. This is consistent with previous results predicting density independent transitions in cell monolayers at critical cell shape parameters [6, 9]; the reduced shear deformation indicates more isotropic shape of each cell, which corresponds to reduced cell aspect ratio and shape index in confluent systems. To further test this intuition, we performed measurements on cells that had undergone EMT and found that restrictions in volumetric deformations still occur, suggesting a gas-liquid transition can occur, whereas restrictions in shear deformation are ablated, suggesting jamming does not occur (Fig. 3-7). Such a result is consistent with recent findings that EMT and jamming/unjamming offer distinct pathways to collective cellular motion [43].

3.5 Epithelial versus Mesenchymal Cell Monolayers

EMT is a process that has significant physiological and pathological relevance, occurring in tissue repair, embryogenesis, and cancer invasion[33]. To further test the applicability of our new order parameters, we use volumetric and shear order parameters to investigate changes in structural order associated with cells that have undergone EMT. To do so, we follow an established protocol to induce EMT by treating human mammary epithelial cells MCF-10A with $10\,\mathrm{ng\,mL^{-1}}$ $TGF\beta1$ for one week [30]. We then culture both the control and $TGF\beta1$ treated cells on 2D glass substrates coated with $0.1\,\mathrm{mg\,mL^{-1}}$ collagen I, at a low cell density $\sim 100\,\mathrm{mm^{-2}}$ (Figs. 3-7A&B), and allow them to grow and reach confluency over time. Cells are trans-

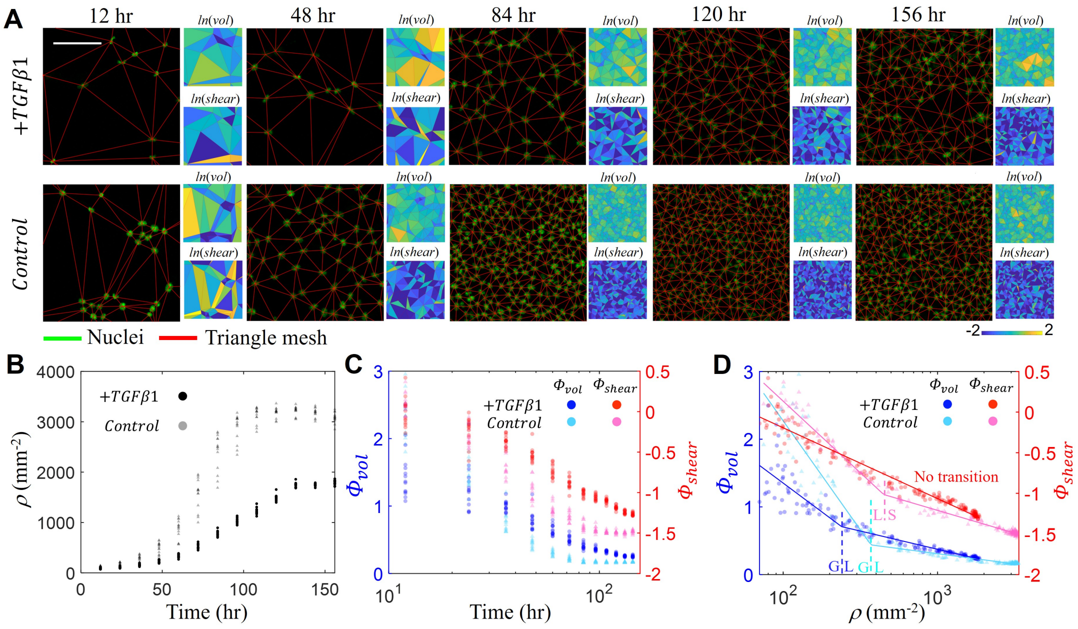

Figure 3-7: Amorphous transition in Φ_{shear} vanishes in MCF-10A monolayer after induction of EMT. (A) Cell nuclei, triangle mesh, and distribution of *vol* and *shear* of both TGFβ1 treated and control group. Scale bar, 100 µm. (B) Density as a function of time. (C) Φ_{vol} and Φ_{shear} as functions of time. (D) Φ_{vol} and Φ_{shear} as functions of cell density. Changes in the scaling behavior of both Φ_{vol} and Φ_{shear} are evident in the control as density increases, while only a change in Φ_{vol} is observed in the $TGF\beta1$ treated monolayer as cell density increases. Transitions in scaling behavior are annotated to mark changes in material phases. G: gas-like phase; L: liquid-like phase; S: solid-like phase.

fected with GFP-NLS for visualizing their nuclei. These cells are imaged every 12 hours until cell density reaches a plateau (Fig. 3-7B); the observed cell density change over time follows a typical S-shaped growth curve. At low density, mesenchymal-like cells in the TGFβ1 treated group move rather individually and thus are more evenly distributed, while the control group of epithelial cells are clearly clustered (Fig. 3-7A, 12hr); indeed, we find that Φ_{vol} of the TGFβ1 treated group is smaller than the control (Fig. 3-7C). As the monolayers develop, both Φ_{vol} and Φ_{shear} of the control group drastically decrease while those of the TGFβ1 treated cells more slowly decrease (Fig. 3-7C). At the end of experiments, 156 hours after seeding, both Φ_{vol} and Φ_{shear} of the TGFβ1 treated cells remain larger than the control, indicating larger density fluctuation and amorphousness, which can also be observed from the fluorescent images (Fig. 3-7A, 156 hr). Interestingly, while TGFβ1 treatment makes MCF-10A cells more mesenchymal-like (Fig. B-2), it also slows down their division (Fig. 3-7B) [14, 16]. As a result, we plot Φ_{vol} and Φ_{shear} against cell density: We find that curves of the two groups do not collapse (Fig. 3-7D), indicating an intrinsic difference in the dynamics of the two groups. Abrupt changes in power-law scaling of Φ_{vol} are observed for both the TGFβ1 treated and control groups, suggesting a gas-liquid transition in density fluctuation occurs in both groups. Interestingly, a change in power-law scaling of Φ_{shear}, an indicator of liquid-solid transition in amorphousness, is only observed in the control and no transition in scaling is observed for the TGFβ1 treated group. These results suggest that the TGFβ1 treated group only has gas-like and liquid-like phases, while all the three phases are observed in the control.

3.6 Invasive versus Non-invasive Epithelial Clusters

While 2D cell monolayers such as epithelia widely exist in nature, cells are mostly organized in a 3D space in tissues and organs. To examine if volumetric and shear order parameters can also describe changes in material characteristics in 3D multicellular systems, we investigate invasion process of epithelial spheroids in 3D. To do so, we grow human mammary epithelial spheroids from MCF-10A cells in an interpenetrating gel containing $5\,\mathrm{mg\,mL^{-1}}$ alginate and $4\,\mathrm{mg\,mL^{-1}}$ Matrigel. These cells form a spheroid shape in the first several days after seeding (Fig. 3-8A top) and become invasive and migrate into the surrounding matrix in about 7 to 10 days (Fig. 3-8A bottom); this system has been previously used to model tumor invasion [15, 47, 37]. To visualize individual cell nuclei, we transfect these cells to express GFP-NLS. Using these nuclear positions, we calculate volumetric and shear order parameters in 3D. Interestingly, comparing to non-invasive spheroids (day 5), we find that invasive spheroids (day 10) have no significant difference in Φ_{shear} but much larger Φ_{vol} (Fig. 3-8D); both order parameters are far from the baseline values of a face-centered cubic crystal. This indicates that while both invasive and non-invasive spheroids are highly amorphous, there is no significant difference in the degree of amorphousness, but the

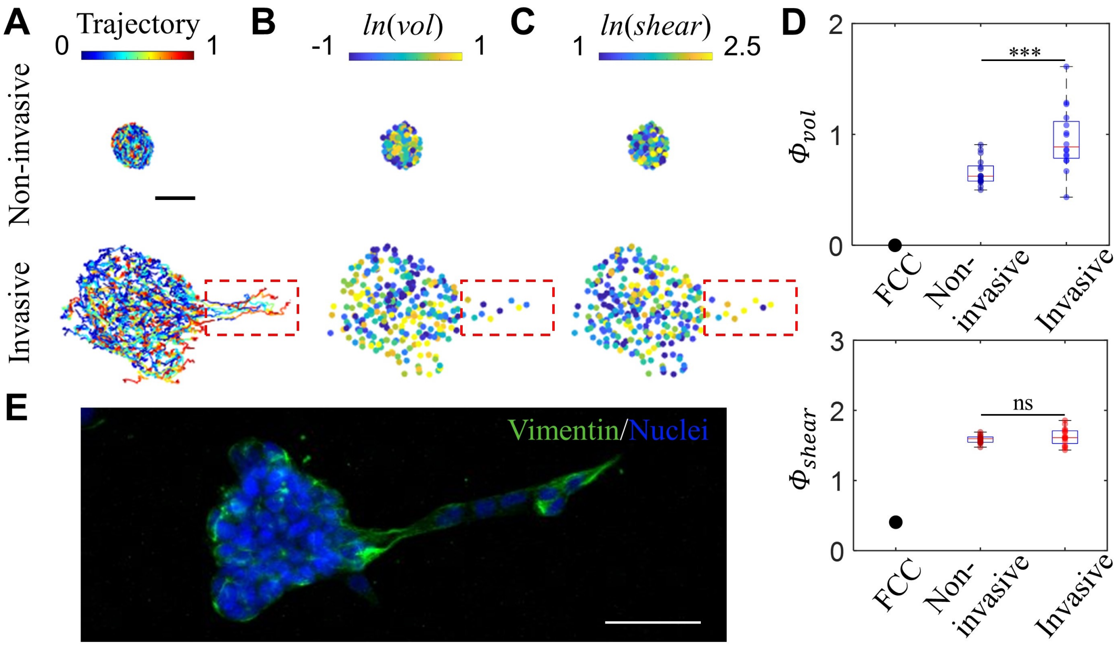

Figure 3-8: Invasive epithelial spheroids have larger density variations but no significant difference in amorphousness. (A) Typical cell trajectories. (B)-(C) Typical spatial distribution of *vol* (B) and *shear* (C). Dash box: the protrusion has more dynamic cells, larger shear deformation but similar volumetric deformation compared to the core. Scale bar, 50 µm. (D) Φ_{vol} and Φ_{shear} of non-invasive ($n = 17$) and invasive spheroids ($n = 16$). While volumetric order is significantly higher for invasive spheroids, shear order for both invasive and non-invasive spheroids are similarly large. Both order parameters deviate far from face-centered cubic crystalline structure. Student's t-test is used to evaluate statistical difference. $* * * : p < 0.001$; ns: no significant difference. FCC: face-centered cubic crystal structure. (E) Fluorescent imaging of vimentin intermediate filaments and nuclei. Scale bar, 50 µm.

invasive spheroids have a much larger density variation. If making an analogy with classical thermal phases, where the solid-liquid transition is mainly due to changes in amorphousness, and the liquid-gas transition is mainly due to changes in density variation, the transition from non-invasive spheroids to invasive ones are not only analogous to fluidization, but more specifically from liquid-like to gas-like. Furthermore, comparing to the core of the spheroid, we find that cells in the protrusion have larger *shear* but not obviously different *vol* (Figs. 3-8B&C), suggesting that the invasive protrusions are more distorted compared to the core. The branch having a larger *shear* is consistent with the spatial distribution of cell behaviors from the trajectories where we find that cells move collectively toward the invasive protrusion (Fig. 3-8A, bottom). This suggests that cells need to deform and squeeze as a collective group to invade into the surrounding matrix. This partially validates the previous hypothesis that confinement of the matrix is a key resistance that migratory cells confront to break away from the original cluster [32, 23], and the fact that leader cells in collective migration often have a more elongated mesenchymal shape [22]. Interestingly, as we perform immunofluorescent imaging of vimentin, a type of intermediate filament that is upregulated during EMT, we find that vimentin is indeed upregulated in the invasive branches (Fig. 3-8E). Thus a possible explanation for invasive spheroids becoming more disordered is that loss of intercellular adhesion as a result of EMT may lead to unjamming of a cellular collective [36]. To summarize, the spatial and temporal changes of volumetric and shear order suggest that invasive mammary epithelial spheroids can tune their material properties to colonize new territories and remodel their configuration.

Chapter 4

Probability Distributions of Volume and Shear

While spatial organization of cells is intrinsically a stochastic process that requires a balance between entropy and some energy-like quantity, the thermodynamic measure of temperature and entropy is irrelevant, and a proper definition of entropy and temperature is needed. To understand cell packing, one may seek to borrow ideas from granular physics. In the famous Edwards volume ensemble theory, the volume is considered as the energy-like quantity, which yields a granular temperature, compactivity [19]. This concept is useful yet not complete, as volume-independent transition is also crucial in multicellular assemblies [9]; Edwards himself pointed out in his original paper that other quantities may be needed to determine the states for other types of external loading such as isochoric shearing [19], and others noted lately that the volume ensemble fails to discriminate among many different microstates [12]. On the other side of the theory, the angoricity tensor, a tensorial effective temperature, was also proposed by considering force and moment balance on grains [8]. While the angoricity tensor accounts for both isotropic and isochoric stresses, it is not trivial to measure stresses experimentally in a living system, so a configurational entropy and temperature from geometries are still in some sense preferable. However, it remains elusive what are the state variables, or even how many state variables are needed to quantify the microstates and configurational entropy of a living system. Here we seek to use the two invariants J and γ to define the local microstates of multicellular living systems.

4.1 Simulated Epithelia

We first examine the probability distribution of γ and J in a simulated cell monolayer by the SPV model [10]. Previous study has demonstrated by quantifying effective diffusivity that systems with a target shape index p below 3.81 is solid-like, while above is fluid-like [10]. Interestingly, here we find that the probability of γ can be well fitted to an exponential distribution $p(\gamma) = \lambda e^{-\lambda\gamma}$, and the probability of normalized area $J^* = \frac{J-J_{min}}{<J>-J_{min}}$ can be fitted to a $k-\Gamma$ distribution that $p(J^*) = k^k {J^*}^{k-1} e^{-kJ^*}/\Gamma(k)$, regardless of the system being fluid-like or solid-like (Fig. 4-1).

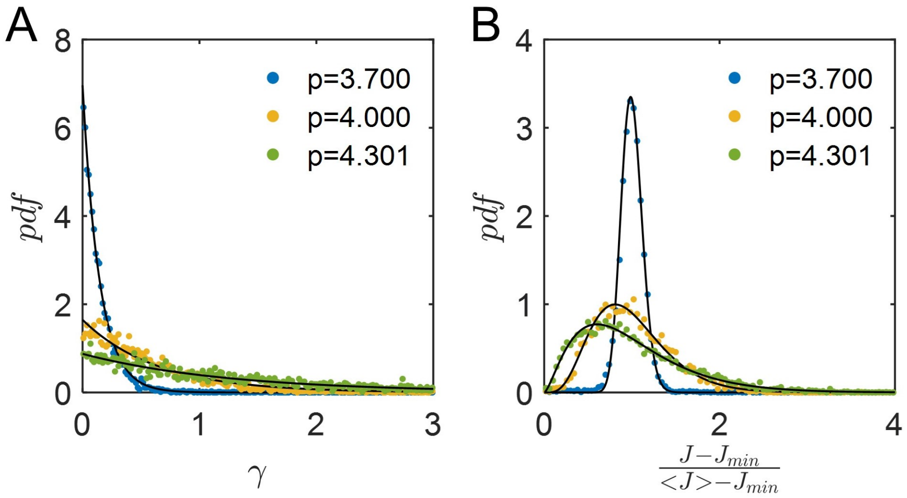

Figure 4-1: In simulated cell monolayers, (A) γ follows exponential distribution (the solid lines are exponential fit); (B) J follows $k-\Gamma$ distribution (the solid lines are $k-\Gamma$ fit).

4.2 Maturation of Epithelia

We then move to real epithelia to examine such two probability distributions of γ and J. MDCK cells with GFP-NLS are cultured on collagen coated glass substrate, with fluorescent cell nuclei that allow us to locate individual cells and perform Delaunay

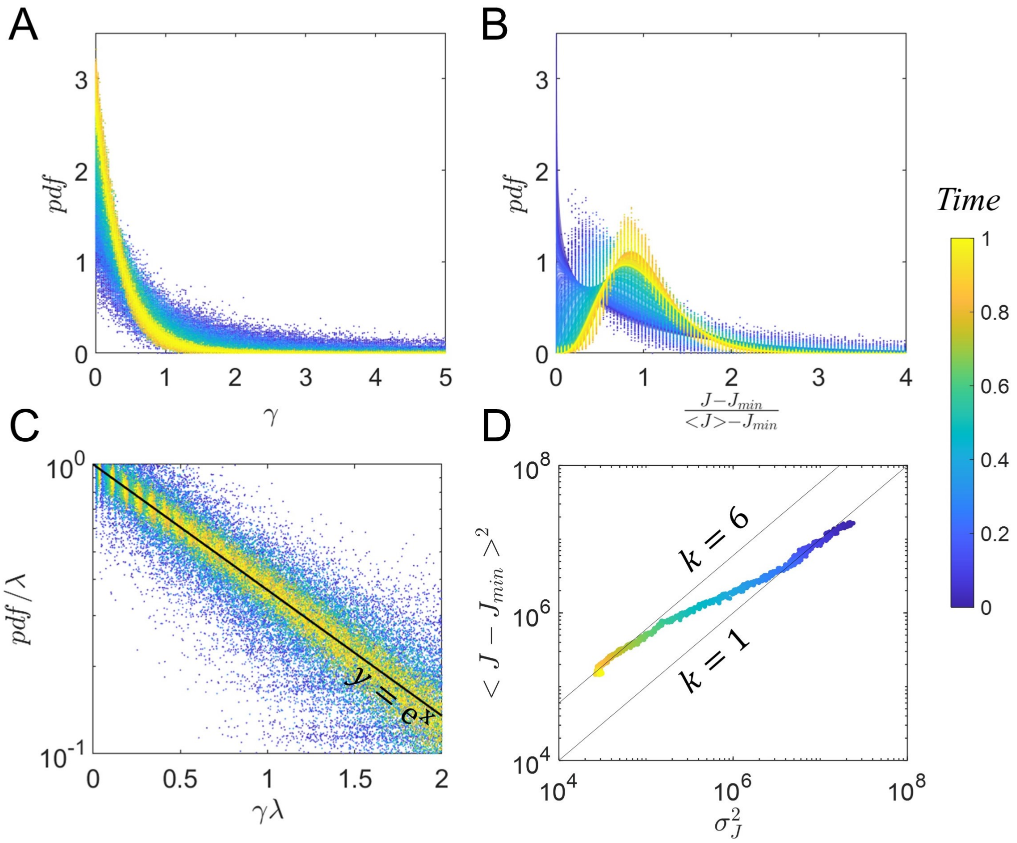

Figure 4-2: (A) γ follows exponential distribution; (B) J follows $k-\Gamma$ distribution in MDCK epithelia. Solid lines are fitted curves. (C) Probability distribution of γ can be collapsed to a single master curve, confirming the exponential distribution of γ at all different cell densities. (D) Average value of $J - J_{min}$ as a function of the variance of J. The coefficient k of the $k - \Gamma$ distribution can be calculated by $k = (< J - J_{min} >^2)/{\sigma_J}^2$. The two lines mark $k = 1$ and $k = 6$ respectively. The total length of the observation is 164 hours. Color bar indicates a dimensionless pseudo time.

triangulation. The cells are seeded sparsely but they divide to reach confluency and eventually jamming at the end of the observation. Surprisingly, we find that the exponential distribution of $p(\gamma)$ and the $k - \Gamma$ distribution of $p(J^*)$ hold for the epithelia at all densities throughout the experiment (Fig. 4-2A&B). To further validate the exponential distribution in γ, we normalize γ and the probability density to show that probability density of systems at all different densities can be collapsed to the master curve (Fig. 4-2C). The $k - \Gamma$ distributions of J are not always similar, but possess a variety of shapes determined by the parameter k. It can be shown that at the beginning of the experiment when the cells are comparably sparse, k is close to

1, while at the end of the experiment k is close to 6 (Fig. 4-2D). Because k indicates the level of correlation of a unit with its neighbors [5], this result is intuitive that a crowded system show spatial volume correlations while a sparse system has no such correlation.

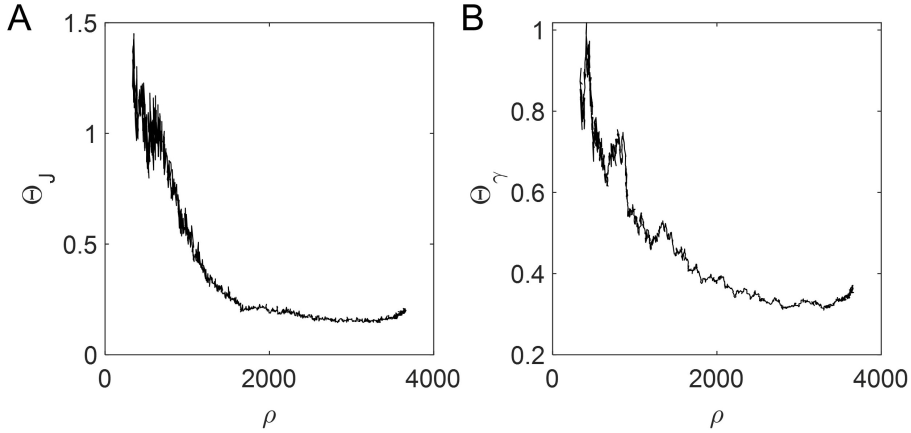

Figure 4-3: Evolution of the two effective temperatures (A) Θ_J and (B) Θ_γ as functions of cell number density ρ.

The $k - \Gamma$ distribution in J^* is expected within the Edwards framework, that the volume ensembles should all fall into such distribution regardless of the segmentation method [5], and the number k indicates the volume of the chosen elements consists of the volume of k more fundamental elements. Moreover, defining an effective temperature to be $\frac{\partial entropy}{\partial energy}$ yields $\frac{<J>-J_{min}}{k}$ [5]. Here, by considering the dimensionless area $J^* = \frac{J-J_{min}}{<J>-J_{min}}$, we get the volume temperature $\Theta_J = k^{-1}$. On the other hand, there is currently no formal theory on the exponential distribution of γ, however, one may argue that besides the Edwards volume ensemble that the isotropic shape J is an effective energy for a grain, the isochoric shape γ can be treated as another independent effective energy, which makes λ^{-1} reminiscent of a second temperature $\Theta_\gamma = \lambda^{-1}$. This is aligned with previous study where shape of Voronoi cells is proposed to be an effective energy-like quantity in epithelia [6]. The evolution of such two temperatures is shown in Fig. 4-3. It is worth noting that because the fundamental objects are triangles with two degrees of freedom in their shapes, this pair of temperatures derived from the two independent invariants thus form a complete description of the variations in microstates.

4.3 Extravasation into Open Space

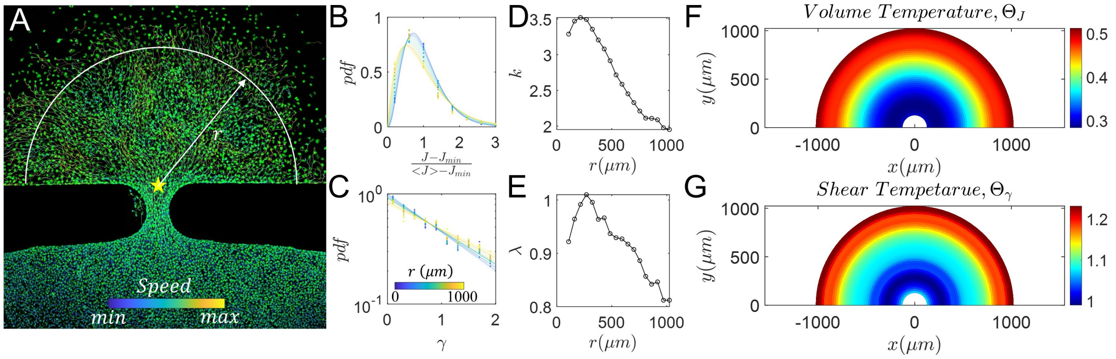

Figure 4-4: The periphery of an epithelia colony is 'hotter' compared to the jammed core. (A) Fluorescent image of MCF-10A cells migrating from a confluent confined space through a slit into an open space. The color of overlaid trajectories indicates the average speed of the cell. The cells on the edge move faster. (B)-(C) Probability density functions of J^* and γ. (D)-(E) Radial distribution of k and λ. (F)-(G) Spatial distributions of volume and shear temperatures.

In the pioneer work by Angelini et al. [4] a famous analogy was drawn between the tip of wound in an epithelia and local high temperature zone in molecular glass; later on, a similar analogy is made suggesting that an invasive tumor has higher effective temperature compared to noninvasive ones [34]. Such analogy is attractive yet remains elusive because there was not a proper definition of temperature-like quantities in multicellular systems. Here we seek to explore this conjecture with the two proposed temperatures. We use a 2D microfluidic system to model extravasation: A well with a slit with width $\sim 100\,\mu\text{m}$ is seeded with exceeding number of MCF-10A cells (with GFP-NLS) to ensure confluency (Fig. 4-4A). Once culture media is added to the outside, the cells start to extravasate through the slit. A half circular colony is gradually established. We analyze the radial pattern by dividing the circular colony into bins of radii. Remarkably, at all different radii ranges, the $k - \Gamma$ distribution in J^* and the exponential distribution in γ are observed (Fig. 4-4B&C). k decays with radius indicating a smaller volume correlation and a larger volume variation in the periphery (Fig. 4-4D), this is consistent with the radial profile of the variance in the divergence of velocity field (FIG. B-3). λ decays with radius, indicating larger probability of observing irregular triangles (Fig. 4-4E). The spatial distribution of volume and shear temperatures shows larger variations in both size and shape in the periphery, in which sense the periphery is indeed ‘hotter’ than the core (Fig. 4-4F&G).

Chapter 5

Summary and Outlook

We quantify the local order in multicellular assemblies by volume and shear. In chapter 3, we define two new order parameters, volumetric order Φ_{vol} and shear order Φ_{shear} to quantify the structure among neighboring cells in multicellular living systems. Φ_{vol} and Φ_{shear} form a complete description of structural order; Φ_{vol} describes the degree of density disorder which reflects factors such as non-confluency (Figs. 3-2,3-6, and 3-8) and size/density heterogeneity (Figs. 3-2,3-4, and 3-6), while Φ_{shear} characterizes packing disorder resulted from factors such as jamming transition (Figs. 3-2,3-3,3-4, and 3-6) and anisotropic cell shapes (Figs. 3-4,3-6, and 3-8). We first show that Φ_{vol} and Φ_{shear} can describe phase transitions in particulate systems. Interestingly, once jamming is initiated, Φ_{shear} scales with internal pressure (Fig. 3-2E), which suggests a potential noninvasive measurement of stress from only static images. Then we demonstrate that Φ_{shear} alone is equivalent to shape index in determining the jamming phase boundary in SPV simulations of confluent cell monolayer. Moreover, we identify two scaling regimes during Drosophila embryogenesis, and show that previously observed elongation of individual cells is resulted from not only changes in packing, but also changes in volume of the space among neighboring cells (Fig. 3-4). We further show the importance of Φ_{vol} in studying those nonconfluent living systems. Applying this framework to a growing epithelial monolayer reveals a gas-like state of monolayers below confluency, a liquid-like state upon monolayer maturation, and then a solid-like state when the monolayer is jammed (Fig. 3-6). Interestingly, we also find that induction of EMT changes the power-law scaling in both Φ_{vol} and Φ_{shear} as functions of cell density (Fig. 3-7). Finally, with this framework, we find that invasive 3D human mammary epithelial spheroids have significantly larger density variation Φ_{vol}, but no significant difference in the degree of amorphousness Φ_{shear} than their noninvasive counterparts; moreover, particularly high shear deformations are observed in the invasive branches (Fig. 3-8). In chapter 4, we discuss the probability distribution of volume and shear and show that the volume follows a $k-\Gamma$ distribution while the shear follows an exponential distribution in SPV simulations (Fig. 4-1), across a large range of cell number densities during the maturation of MDCK epithelia (Fig. 4-2), and at different radial locations during the extravasation of MCF-10A epithelia (Fig. 4-4). We further show that a pair of temperature-like quantities can be extracted from the exponential tails of the probability distributions (Fig. 4-3), in which sense the periphery of an extravasating epithelial colony is 'hotter' than the core (Fig. 4-4).

An intriguing question in cell mechanobiology is how tissue level order emerges within a group of cells. It is known that it starts from single cell scale, regulated by genetics and cell signaling, and manifests at the tissue and organ scale setting tissue morphology, rigidity, function, etc. However, a structural description between the two length scales remains elusive; indeed, while local interaction of a cell with its close neighbors plays a critical role in regulating material characteristics of tissues, it has been difficult to characterize this interaction, particularly *in situ*. Thus, the framework introduced here may reveal important structural information that was not previously accessible during processes such as wound healing and cancer metastasis. Furthermore, this methodology could be used to monitor how structural characteristics are influenced by mechanical or biochemical perturbations.

We expect that this method may provide a morphological assay for histopathology evaluation. In traditional histopathology, individual cell morphology and tissue structure are two main features typically being examined. Breast cancer grade, for example, is determined based on nuclear pleomorphism, cell division, and gland or tubule formation [25]. However, there is growing evidence from *in vitro* experiments showing that intercellular interactions such as formation of gap junctions are also important for invasion in epithelial derived model tumor spheroids [27]. The volume and shear structures reveal clear geometrical information of the local structure among neighboring cells that was missing in previous morphological assays; this method can be readily incorporated into existing diagnostic pipelines and might serve as an additional marker for diagnosis. As this method is solely based on analyzing static images, it can be readily applied to histopathological data with simple staining method visualizing cell positions, such as biopsy samples with stained cell nuclei.

The framework we introduce here is general and unified, such that can be applied to systems both on 2D and in 3D, and to both confluent and dispersed multicellular systems. Based on cell locations, we can characterize material phases and identify important changes in materials states that may contribute to important biological processes of the tissue. Using this framework, we can resolve details in evolution of material characteristics starting from extremely low density to full confluency and eventually jammed states. The generality and robustness of this framework allows different systems to be compared in a consistent way.

Appendix A

Lemmas

Lemma 1: *vol* and *shear* are independent of the orientation of the reference triangle.

Proof: Consider an arbitrary rotation $\mathbf{Q}$ of the initial reference $\mathbf{T_r}$, the new triangle may be written as $\mathbf{T_r^*} = \mathbf{QT_r}$. The new deformation gradient is $\mathbf{F_n^*} = \mathbf{T_n T_r^{-1} Q^T}$.The new volumetric deformation is

$$\begin{aligned} vol^* &= det(\mathbf{T_n T_r^{-1} Q^T}) \\ &= det(\mathbf{T_n T_r^{-1}}) \\ &= vol \end{aligned}$$

The trace of $\mathbf{F^{*T} F^*}$ is

$$\begin{aligned} tr(\mathbf{F^{*T} F^*}) &= tr(\mathbf{F^* F^{*T}}) \\ &= tr((\mathbf{T_n T_r^{-1} Q^T})(\mathbf{T_n T_r^{-1} Q^T})^\mathbf{T}) \\ &= tr(\mathbf{T_n T_r^{-1} Q^T Q T_r^{-T} T_n^T}) \\ &= tr(\mathbf{T_n T_r^{-1} T_r^{-T} T_n^T}) \\ &= tr(\mathbf{F^T F}) \end{aligned}$$

Thus the new shear deformation is $shear^* = shear$.

The lemmas 2 and 3 are to prove that the *vol* and *shear* represent the real volumetric and shear deformations of each individual triangle compared with the referential average equilateral triangle in Cartesian coordinate.

Lemma 2: An arbitrary 2D deformation gradient $\mathbf{F}$ can be factored into a pure volumetric deformation and a simple shear deformation as $\mathbf{F} = \mathbf{F_v}\mathbf{F_s}$, where $\mathbf{F_v} = (\lambda_1\lambda_2)^{1/2}\mathbf{I}$, and $\mathbf{F_s} = (\sqrt{\frac{\lambda_1}{\lambda_2}} - \sqrt{\frac{\lambda_2}{\lambda_1}})\boldsymbol{e'_1} \otimes \boldsymbol{e'_2} + \mathbf{I}$. $\boldsymbol{e'_1}$, $\boldsymbol{e'_2}$ are orthogonal basis and λ_1, λ_2 are the two eigenvalues of $\mathbf{F}$.

Proof: An arbitrary deformation gradient $\mathbf{F}$ can be factored into two components $\mathbf{F} = \mathbf{F_v}\mathbf{F_s}$, where $\mathbf{F_v} = v\mathbf{I} = (\lambda_1\lambda_2)^{1/2}\mathbf{I}$. Then $\mathbf{F_s}$ is an isochoric deformation with two eigenvalues $\sqrt{\frac{\lambda_1}{\lambda_2}}$ and $\sqrt{\frac{\lambda_2}{\lambda_1}}$. According to Lemma 3, $\mathbf{F_s}$ can be regarded as a simple shear deformation in some basis, and the equivalent amount of shear is $s = \sqrt{\frac{\lambda_1}{\lambda_2}} - \sqrt{\frac{\lambda_2}{\lambda_1}}$. Furthermore, from simple eigenvalue analysis, $v^2 = det(\mathbf{F})$, and $s^2 = \frac{tr(\mathbf{F^T F})}{det(\mathbf{F})} - 2$.

Lemma 3: An arbitrary isochoric 2D deformation gradient $\mathbf{F}$ can be regarded as a simple shear in some basis, with amount of shear $s = \lambda - \frac{1}{\lambda}$,where λ and $\frac{1}{\lambda}$ $(\lambda \geq 1)$ are eigenvalues of $\mathbf{F}$.

Proof: An arbitrary deformation gradient $\mathbf{F}$ can be factored as $\mathbf{F} = \mathbf{QK}$, where $\mathbf{K}$ is the deformation gradient that can be transformed to $\mathbf{F}$ after a rotation $\mathbf{Q}$. Alternatively, the polar decomposition of $\mathbf{F}$ is $\mathbf{F} = \mathbf{RU}$, where $\mathbf{R}$ is a rotation, and $\mathbf{U}$ is diagonal. Thus $\mathbf{F^T F} = (\mathbf{QK})^{\mathbf{T}}\mathbf{QK} = (\mathbf{RU})^{\mathbf{T}}\mathbf{RU}$, which can be further simplified as $\mathbf{K^T K} = \mathbf{U^2}$.The eigenvalue equation of two sides must be identical, and both eigenvalues of two sides need to be equal, leading to two algebraic equations. Assuming that $\mathbf{K}$ can be written as a simple shear in some basis $\mathbf{K} = s\boldsymbol{e'_1} \otimes \boldsymbol{e'_2} + \mathbf{I}$, then for an isochoric deformation gradient $\mathbf{F}$ we have $s^2 + 2 = \lambda^2 + \frac{1}{\lambda^2}$. So $s = \lambda - \frac{1}{\lambda}$. This also proves that such $\mathbf{K}$ and $\mathbf{Q}$ exist.

Appendix B

Supplementary Results

LJ(Lennard-Jones) potential between two particles at distance r is given by $U_{LJ}(r) = 4\epsilon[(\frac{a}{r})^{12} - (\frac{a}{r})^{6}]$, such that it is controlled by only two dimensionless parameters, the dimensionless temperature $T = k_b T_r/\epsilon$, and the dimensionless density $\rho = \rho_r a^2$, where k_b is the Boltzmann constant, T_r is the absolute temperature, ϵ is the potential depth, ρ_r is the number density of particles, a is the separation distance when the bonding energy potential is equal to zero. We perform the simulations with HOOMD-blue [2]. 900 particles with unit radius are initially distributed on 30 by 30 square lattice and area of each square is $\frac{1}{\rho}$. The simulations are run for 2×10^5 steps to reach equilibrium.

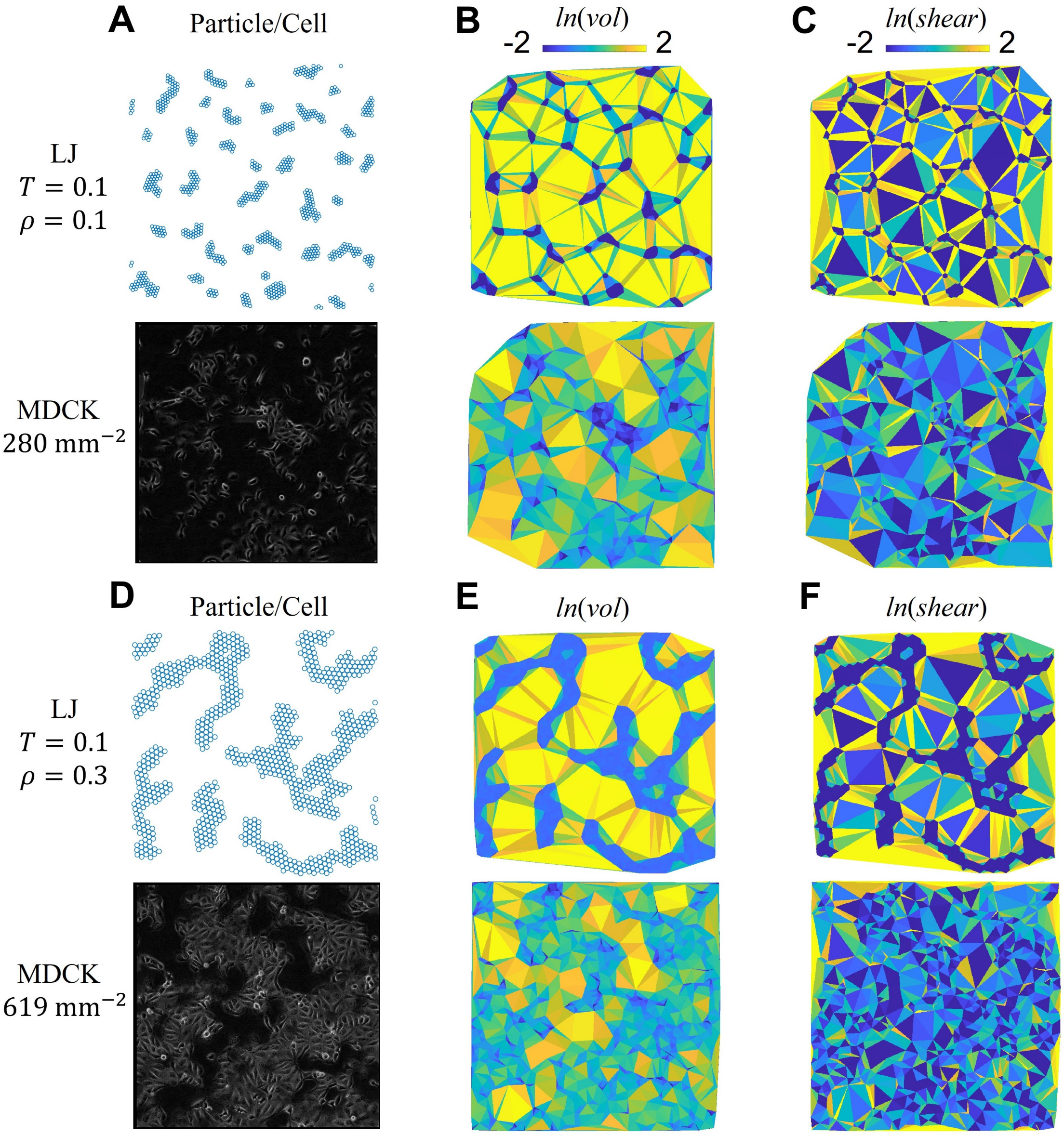

Figure B-1: Behavior of a sparse MDCK epithelial cell monolayer is analogous to the nucleation in sparse LJ system whose potential energy is dominating over kinetic energy, in terms of (A) particle/cell positions; (B) $\ln(vol)$ (C) $\ln(shear)$. With increased particle density, the discrete packs start to aggregate (D). These packs are dense (E), and well packed (F).

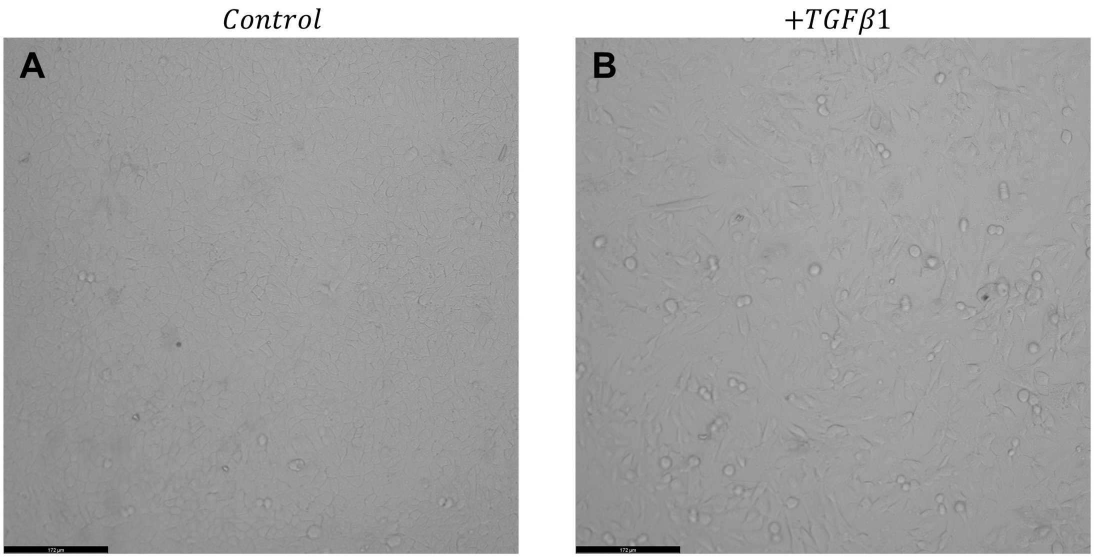
Control
+TGFβ1
A
B
172 µm
172 µm

Figure B-2: Brightfield images of (A) MCF-10A epithelia versus (B) MCF-10A epithelia after induction of EMT.

Because higher variations in cell area is observed at the periphery of the extravasating epithelia, a natural quantity to check will be the variance of the divergence of velocity field. The total area outside the slit is divided into 35 × 70 grids, and the velocity $V = (u, v)^T$ is taken to be the average cell velocity within the grid, where u is the velocity along the x axis and v is the velocity along the y axis. The divergence is calculated by $\nabla \cdot V = \frac{du}{dx} + \frac{dv}{dy}$. The divergence is then registered to bins of radii, and the variance is calculated within each radius range.

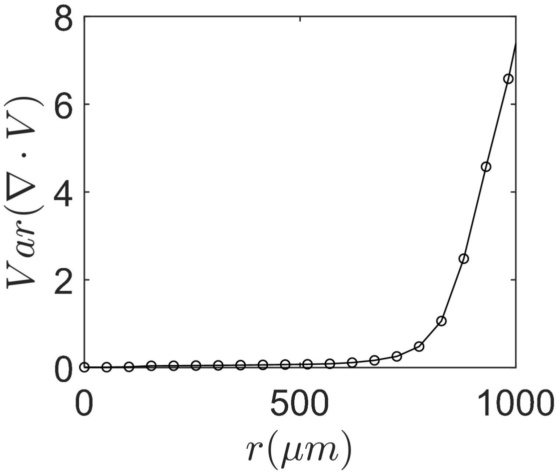

Figure B-3: The variance of divergence of velocity field increases at the periphery of epithelial colony.

Bibliography

[1] Michael P Allen and Dominic J Tildesley. *Computer simulation of liquids*. Oxford university press, 2017.

[2] Joshua A Anderson, Jens Glaser, and Sharon C Glotzer. Hoomd-blue: A python package for high-performance molecular dynamics and hard particle monte carlo simulations. *Computational Materials Science*, 173:109363, 2020.

[3] Thomas E Angelini, Edouard Hannezo, Xavier Trepat, Jeffrey J Fredberg, and David A Weitz. Cell migration driven by cooperative substrate deformation patterns. *Physical review letters*, 104(16):168104, 2010.

[4] Thomas E Angelini, Edouard Hannezo, Xavier Trepat, Manuel Marquez, Jeffrey J Fredberg, and David A Weitz. Glass-like dynamics of collective cell migration. *Proceedings of the National Academy of Sciences*, 108(12):4714–4719, 2011.

[5] Tomaso Aste and Tiziana Di Matteo. Emergence of gamma distributions in granular materials and packing models. *Physical Review E*, 77(2):021309, 2008.

[6] Lior Atia, Dapeng Bi, Yasha Sharma, Jennifer A Mitchel, Bomi Gweon, Stephan A Koehler, Stephen J DeCamp, Bo Lan, Jae Hun Kim, Rebecca Hirsch, et al. Geometric constraints during epithelial jamming. *Nature physics*, 14(6):613–620, 2018.

[7] Katalin Bagi. Analysis of microstructural strain tensors for granular assemblies. *International Journal of Solids and Structures*, 43(10):3166–3184, 2006.

[8] Dapeng Bi, Silke Henkes, Karen E Daniels, and Bulbul Chakraborty. The statistical physics of athermal materials. *Annu. Rev. Condens. Matter Phys*, 6:63–83, 2015.

[9] Dapeng Bi, JH Lopez, Jennifer M Schwarz, and M Lisa Manning. A density-independent rigidity transition in biological tissues. *Nature Physics*, 11(12):1074–1079, 2015.

[10] Dapeng Bi, Xingbo Yang, M Cristina Marchetti, and M Lisa Manning. Motility-driven glass and jamming transitions in biological tissues. *Physical Review X*, 6(2):021011, 2016.

[11] Erik Bitzek, Pekka Koskinen, Franz Gähler, Michael Moseler, and Peter Gumbsch. Structural relaxation made simple. *Physical review letters*, 97(17):170201, 2006.

[12] Raphael Blumenfeld, Shahar Amitai, Joe F Jordan, and Rebecca Hihinashvili. Failure of the volume function in granular statistical mechanics and an alternative formulation. *Physical review letters*, 116(14):148001, 2016.

[13] Agustí Brugués, Ester Anon, Vito Conte, Jim H Veldhuis, Mukund Gupta, Julien Colombelli, José J Muñoz, G Wayne Brodland, Benoit Ladoux, and Xavier Trepat. Forces driving epithelial wound healing. *Nature physics*, 10(9):683–690, 2014.

[14] Anita Buck, Malte Buchholz, Martin Wagner, Guido Adler, Thomas Gress, and Volker Ellenrieder. The tumor suppressor klf11 mediates a novel mechanism in transforming growth factor β–induced growth inhibition that is inactivated in pancreatic cancer. *Molecular cancer research*, 4(11):861–872, 2006.

[15] Ovijit Chaudhuri, Sandeep T Koshy, Cristiana Branco da Cunha, Jae-Won Shin, Catia S Verbeke, Kimberly H Allison, and David J Mooney. Extracellular matrix stiffness and composition jointly regulate the induction of malignant phenotypes in mammary epithelium. *Nature materials*, 13(10):970–978, 2014.

[16] Valentine Comaills, Lilian Kabeche, Robert Morris, Rémi Buisson, Min Yu, Marissa Wells Madden, Joseph A LiCausi, Myriam Boukhali, Ken Tajima, Shiwei Pan, et al. Genomic instability is induced by persistent proliferation of cells undergoing epithelial-to-mesenchymal transition. *Cell reports*, 17(10):2632–2647, 2016.

[17] Michael Czajkowski, Daniel M Sussman, M Cristina Marchetti, and M Lisa Manning. Glassy dynamics in models of confluent tissue with mitosis and apoptosis. *Soft matter*, 15(44):9133–9149, 2019.

[18] Jayanta Debnath, Senthil K Muthuswamy, and Joan S Brugge. Morphogenesis and oncogenesis of mcf-10a mammary epithelial acini grown in three-dimensional basement membrane cultures. *Methods*, 30(3):256–268, 2003.

[19] Sam F Edwards and RBS Oakeshott. Theory of powders. *Physica A: Statistical Mechanics and its Applications*, 157(3):1080–1090, 1989.

[20] Gonca Erdemci-Tandogan, Madeline J Clark, Jeffrey D Amack, and M Lisa Manning. Tissue flow induces cell shape changes during organogenesis. *Biophysical journal*, 115(11):2259–2270, 2018.

[21] Raphaël Etournay, Marko Popović, Matthias Merkel, Amitabha Nandi, Corinna Blasse, Benoît Aigouy, Holger Brandl, Gene Myers, Guillaume Salbreux, Frank Jülicher, et al. Interplay of cell dynamics and epithelial tension during morphogenesis of the drosophila pupal wing. *Elife*, 4:e07090, 2015.

[22] Peter Friedl and Darren Gilmour. Collective cell migration in morphogenesis, regeneration and cancer. *Nature reviews Molecular cell biology*, 10(7):445–457, 2009.

[23] Peter Friedl and Katarina Wolf. Plasticity of cell migration: a multiscale tuning model. *Journal of Cell Biology*, 188(1):11–19, 2010.

[24] Matthew C Gibson, Ankit B Patel, Radhika Nagpal, and Norbert Perrimon. The emergence of geometric order in proliferating metazoan epithelia. *Nature*, 442(7106):1038–1041, 2006.

[25] Armando E Giuliano, James L Connolly, Stephen B Edge, Elizabeth A Mittendorf, Hope S Rugo, Lawrence J Solin, Donald L Weaver, David J Winchester, and Gabriel N Hortobagyi. Breast cancer—major changes in the american joint committee on cancer eighth edition cancer staging manual. *CA: a cancer journal for clinicians*, 67(4):290–303, 2017.

[26] Boris Guirao, Stéphane U Rigaud, Floris Bosveld, Anaïs Bailles, Jesús López-Gay, Shuji Ishihara, Kaoru Sugimura, François Graner, and Yohanns Bellaïche. Unified quantitative characterization of epithelial tissue development. *Elife*, 4:e08519, 2015.

[27] Yu Long Han, Adrian F Pegoraro, Hui Li, Kaifu Li, Yuan Yuan, Guoqiang Xu, Zichen Gu, Jiawei Sun, Yukun Hao, Satish Kumar Gupta, et al. Cell swelling, softening and invasion in a three-dimensional breast cancer model. *Nature physics*, 16(1):101–108, 2020.

[28] Evan Hohlfeld and Lakshminarayanan Mahadevan. Unfolding the sulcus. *Physical review letters*, 106(10):105702, 2011.

[29] A Gerhard Holzapfel. *Nonlinear solid mechanics II.* John Wiley & Sons, Inc., 2000.

[30] Kamran Hosseini, Anna Taubenberger, Carsten Werner, and Elisabeth Fischer-Friedrich. Emt-induced cell-mechanical changes enhance mitotic rounding strength. *Advanced Science*, 7(19):2001276, 2020.

[31] Atsushi Ikeda, Ludovic Berthier, and Peter Sollich. Unified study of glass and jamming rheology in soft particle systems. *Physical review letters*, 109(1):018301, 2012.

[32] Olga Ilina, Pavlo G Gritsenko, Simon Syga, Jürgen Lippoldt, Caterina AM La Porta, Oleksandr Chepizhko, Steffen Grosser, Manon Vullings, Gert-Jan Bakker, Jörn Starruß, et al. Cell–cell adhesion and 3d matrix confinement determine jamming transitions in breast cancer invasion. *Nature cell biology*, 22(9):1103–1115, 2020.

[33] Raghu Kalluri, Robert A Weinberg, et al. The basics of epithelial-mesenchymal transition. *The Journal of clinical investigation*, 119(6):1420–1428, 2009.

[34] Wenying Kang, Jacopo Ferruzzi, Catalina-Paula Spatarelu, Yu Long Han, Yasha Sharma, Stephan A Koehler, Jennifer A Mitchel, Adil Khan, James P Butler, Darren Roblyer, et al. A novel jamming phase diagram links tumor invasion to non-equilibrium phase separation. *Iscience*, 24(11):103252, 2021.

[35] Philipp J Keller. Imaging morphogenesis: technological advances and biological insights. *Science*, 340(6137):1234168, 2013.

[36] Caterina AM La Porta and Stefano Zapperi. Phase transitions in cell migration. *Nature Reviews Physics*, 2(10):516–517, 2020.

[37] Kandice R Levental, Hongmei Yu, Laura Kass, Johnathon N Lakins, Mikala Egeblad, Janine T Erler, Sheri FT Fong, Katalin Csiszar, Amato Giaccia, Wolfgang Weninger, et al. Matrix crosslinking forces tumor progression by enhancing integrin signaling. *Cell*, 139(5):891–906, 2009.

[38] Shao-Zhen Lin, Yue Li, Jing Ji, Bo Li, and Xi-Qiao Feng. Collective dynamics of coherent motile cells on curved surfaces. *Soft Matter*, 16(12):2941–2952, 2020.

[39] Andrea J Liu and Sidney R Nagel. The jamming transition and the marginally jammed solid. *Annu. Rev. Condens. Matter Phys*, 1(1):347–369, 2010.

[40] Chiara Malinverno, Salvatore Corallino, Fabio Giavazzi, Martin Bergert, Qingsen Li, Marco Leoni, Andrea Disanza, Emanuela Frittoli, Amanda Oldani, Emanuele Martini, et al. Endocytic reawakening of motility in jammed epithelia. *Nature materials*, 16(5):587–596, 2017.

[41] John C Mauro, Yuanzheng Yue, Adam J Ellison, Prabhat K Gupta, and Douglas C Allan. Viscosity of glass-forming liquids. *Proceedings of the National Academy of Sciences*, 106(47):19780–19784, 2009.

[42] Matthias Merkel and M Lisa Manning. A geometrically controlled rigidity transition in a model for confluent 3d tissues. *New Journal of Physics*, 20(2):022002, 2018.

[43] Jennifer A Mitchel, Amit Das, Michael J O'Sullivan, Ian T Stancil, Stephen J DeCamp, Stephan Koehler, Oscar H Ocaña, James P Butler, Jeffrey J Fredberg, M Angela Nieto, et al. In primary airway epithelial cells, the unjamming transition is distinct from the epithelial-to-mesenchymal transition. *Nature communications*, 11(1):1–14, 2020.

[44] Alessandro Mongera, Payam Rowghanian, Hannah J Gustafson, Elijah Shelton, David A Kealhofer, Emmet K Carn, Friedhelm Serwane, Adam A Lucio, James Giammona, and Otger Campàs. A fluid-to-solid jamming transition underlies vertebrate body axis elongation. *Nature*, 561(7723):401–405, 2018.

[45] Peter Olsson and Stephen Teitel. Critical scaling of shear viscosity at the jamming transition. *Physical review letters*, 99(17):178001, 2007.

[46] Corey S O'hern, Leonardo E Silbert, Andrea J Liu, and Sidney R Nagel. Jamming at zero temperature and zero applied stress: The epitome of disorder. *Physical Review E*, 68(1):011306, 2003.

[47] Matthew J Paszek, Nastaran Zahir, Kandice R Johnson, Johnathon N Lakins, Gabriela I Rozenberg, Amit Gefen, Cynthia A Reinhart-King, Susan S Margulies, Micah Dembo, David Boettiger, et al. Tensional homeostasis and the malignant phenotype. *Cancer cell*, 8(3):241–254, 2005.

[48] Marzia Rovere, Dieter W Heermann, and Kurt Binder. The gas-liquid transition of the two-dimensional lennard-jones fluid. *Journal of Physics: Condensed Matter*, 2(33):7009, 1990.

[49] Monirosadat Sadati, Nader Taheri Qazvini, Ramaswamy Krishnan, Chan Young Park, and Jeffrey J Fredberg. Collective migration and cell jamming. *Differentiation*, 86(3):121–125, 2013.

[50] Preeti Sahu, Daniel M Sussman, Matthias Rübsam, Aaron F Mertz, Valerie Horsley, Eric R Dufresne, Carien M Niessen, M Cristina Marchetti, M Lisa Manning, and Jen M Schwarz. Small-scale demixing in confluent biological tissues. *Soft Matter*, 16(13):3325–3337, 2020.

[51] Balint Szabo, GJ Szöllösi, B Gönci, Zs Jurányi, David Selmeczi, and Tamás Vicsek. Phase transition in the collective migration of tissue cells: experiment and model. *Physical Review E*, 74(6):061908, 2006.

[52] Dhananjay T Tambe, C Corey Hardin, Thomas E Angelini, Kavitha Rajendran, Chan Young Park, Xavier Serra-Picamal, Enhua H Zhou, Muhammad H Zaman, James P Butler, David A Weitz, et al. Collective cell guidance by cooperative intercellular forces. *Nature materials*, 10(6):469–475, 2011.

[53] Jean-Yves Tinevez, Nick Perry, Johannes Schindelin, Genevieve M Hoopes, Gregory D Reynolds, Emmanuel Laplantine, Sebastian Y Bednarek, Spencer L Shorte, and Kevin W Eliceiri. Trackmate: An open and extensible platform for single-particle tracking. *Methods*, 115:80–90, 2017.

[54] Veronique Trappe, V Prasad, Luca Cipelletti, PN Segre, and David A Weitz. Jamming phase diagram for attractive particles. *Nature*, 411(6839):772–775, 2001.

[55] Xavier Trepat and Erik Sahai. Mesoscale physical principles of collective cell organization. *Nature Physics*, 14(7):671–682, 2018.

[56] Ritvik Vasan, Mary M Maleckar, C David Williams, and Padmini Rangamani. Dlite uses cell-cell interface movement to better infer cell-cell tensions. *Biophysical journal*, 117(9):1714–1727, 2019.

[57] Tamás Vicsek, András Czirók, Eshel Ben-Jacob, Inon Cohen, and Ofer Shochet. Novel type of phase transition in a system of self-driven particles. *Physical review letters*, 75(6):1226, 1995.

[58] Dmitri Volfson, Scott Cookson, Jeff Hasty, and Lev S Tsimring. Biomechanical ordering of dense cell populations. *Proceedings of the National Academy of Sciences*, 105(40):15346–15351, 2008.

[59] Hui Wang, Sam Lacoche, Ling Huang, Bin Xue, and Senthil K Muthuswamy. Rotational motion during three-dimensional morphogenesis of mammary epithelial acini relates to laminin matrix assembly. *Proceedings of the National Academy of Sciences*, 110(1):163–168, 2013.

[60] Xun Wang, Matthias Merkel, Leo B Sutter, Gonca Erdemci-Tandogan, M Lisa Manning, and Karen E Kasza. Anisotropy links cell shapes to tissue flow during convergent extension. *Proceedings of the National Academy of Sciences*, 117(24):13541–13551, 2020.

[61] Hiroshi Watanabe, Nobuyasu Ito, and Chin-Kun Hu. Phase diagram and universality of the lennard-jones gas-liquid system. *The Journal of chemical physics*, 136(20):204102, 2012.

[62] Taeseok Daniel Yang, Hyun Kim, Changhyeong Yoon, Seung-Kuk Baek, and Kyoung J Lee. Collective pulsatile expansion and swirls in proliferating tumor tissue. *New Journal of Physics*, 18(10):103032, 2016.